



Full length article

Structural impact of niobium oxide on lithium silicate glasses: Results from advanced interaction-selective solid-state nuclear magnetic resonance and Raman spectroscopy

Henrik Bradtmüller ^{a,*}, Qiuju Zheng ^b, Anuraag Gaddam ^c, Hellmut Eckert ^c, Edgar D. Zanotto ^a

^a Vitreous Materials Laboratory, Department of Materials Engineering, Federal University of São Carlos, CP 676, São Carlos, SP 13565-905, Brazil

^b School of Materials Science and Engineering, Qilu University of Technology, Jinan 250353, China

^c São Carlos Institute of Physics, University of São Paulo, Avenida Trabalhador São Carlense 400, São Carlos, SP 13566-590, Brazil

ARTICLE INFO

ABSTRACT

Keywords:

⁹³Nb
NMR
Glasses
RESPDOR
Spin echo decay
LiNbO₃

While niobium-containing oxide glasses are used in many technological applications, especially optical glasses, the exact structural role of Nb and its impact on the structure of covalent/ionic oxide glasses remain incompletely understood. In the present study, this issue is addressed for Nb₂O₅-containing lithium silicate glasses using ⁷Li, ²⁹Si, and ⁹³Nb magic-angle-spinning (MAS) and advanced NMR methods sensitive to ⁷Li-⁷Li and ⁷Li-⁹³Nb magnetic dipole-dipole interactions, accompanied by molecular dynamics (MD) and Monte-Carlo (MC) simulations. In glasses along the compositional line (1-y)Li₂Si₂O₅-yNb₂O₅, ²⁹Si MAS-NMR spectra reveal a gradual silica network repolymerization with increasing y, indicating that the accommodation of the niobium oxide component into the glassy network requires on average about 0.7 equivalents of lithium oxide. Significant ⁷Li-⁹³Nb interactions were also detected and quantified by Rotational Echo Saturation Pulse Double Resonance (RESPDOR) experiments. Consistent with this finding, profound changes in the local environments of the lithium ions and their spatial distributions are observed in ⁷Li satellite transition (SATRAS) spectra and ⁷Li dipolar spin echo decays, whereas ⁹³Nb NMR and Raman spectra suggest the formation of six-coordinated NbO₆ polyhedra with both, corner- and edge-sharing connectivity. Results obtained on glasses along a second composition line, SiO₂-[(Li₂O)_{1.4}(Nb₂O₅)], confirm the above-described structural concepts. The average homo- and heteronuclear dipolar interaction strengths as expressed by the second moments $M_{2(Li-Li)}$ and $M_{2(Li-Nb)}$ are consistent with random spatial distributions of the lithium and niobium species, with a tendency towards Nb clustering at higher concentrations. All of these results suggest that niobium oxide adopts a *network former* role in these glasses. The current study defines a comprehensive general strategy for elucidating the structural impact of NMR active intermediate oxides incorporated into silicate glasses.

1. Introduction

Niobium oxide (Nb₂O₅) is a common additive used to increase the refractive index of oxide glasses and facilitate a drastic increase in their nonlinear optical (NLO) response, which is essential for optimizing the visual properties of optical elements such as certain electronic displays [1–6]. Applications include augmented reality (also known as mixed reality), smart glasses, and heads-up displays, where the real and digital worlds are mixed by overlaying virtual images on see-through material. Importantly, these applications are achieved without incorporating toxic heavy-metal components such as lead, which is desirable from the environmental and health perspective. Nb₂O₅ is especially important for

ultra-high refractive index ($n_D > 1.8$) glasses, which demand up to 50 wt % of this oxide. Surprisingly, a workable glass-forming ability can still be maintained even with such high content. Niobium oxide is also used to improve the glass-forming ability of optical glasses doped with rare earth elements. These glasses have both good light transmittance and excellent up-conversion luminous efficiency and have broad potential applications in the up-conversion field [7,8]. In addition, niobium-containing glass-ceramics have been used in ferroelectric, piezoelectric, and light-emitting materials due to their high insulation resistance and excellent mechanical strength [9–11]. From the optical devices' perspective, glass ceramics containing nanocrystalline lithium niobate, a material with outstanding electrical and NLO properties, are

* Corresponding author.

E-mail address: mail@bradtmueller.net (H. Bradtmüller).

of great technological interest [12–14].

Despite this substantial technological interest, little is currently known about the effect this transition metal oxide has on the network structure and the network modifier distribution in silicate glasses. In general, Nb_2O_5 is classified as an "intermediate oxide", unable to form a glass by itself under standard preparation conditions, but as a glass formulation component that can act either as a network modifier, creating non-bridging oxygen atoms (NBOs) by breaking oxide linkages between network former units (NFUs), or as a network former species integrating into a three-dimensional aperiodic framework. In this particular role as a network former, niobium may then form negatively charged polyhedra, thus attracting network modifier cations for charge compensation. There seems to be a general literature consensus that niobium in silicate glasses tends to form distorted six-coordinated oxygen polyhedral units due to the second-order Jahn Teller effect [1], as mostly inferred from Raman scattering [15–21] and incipient solid-state NMR data [6,22–28]. However, surprisingly, there is little knowledge about the medium-range order of this oxide, i.e., the connectivities of these niobia polyhedra with those of other network former species and their spatial relations with the network modifiers. Altogether the current understanding of the structural impact of niobia additives upon alkali silicate glasses appears rather incomplete.

The present contribution addresses this issue by means of advanced solid-state NMR spectroscopic methods. Owing to its element selectivity, inherently quantitative character, and its focus on local interactions, solid-state NMR is an ideally suited method for the structural characterization of glasses, where the lack of long-range order precludes a more detailed analysis of diffraction experiments. Although NMR methods have indeed been widely applied to many glasses, to date, the full potential of modern interaction-selective experiments has been under-utilized in the area of niobia-containing glasses. In the present contribution, we develop a comprehensive investigation strategy comprising such experiments. Aside from standard characterization by ^{29}Si , ^7Li , and ^{93}Nb MAS-NMR, we present results from experiments selectively addressing homonuclear and heteronuclear dipole-dipole interactions involving the ^7Li nuclear spins, using ^7Li Hahn spin echo decay spectroscopy and the first-time application of a new version of ^7Li { ^{93}Nb } rotational echo saturation pulse double resonance (RESPDOR) NMR method probing the spatial proximity between lithium and niobium species. The results, interpreted in the context of comparative Molecular Dynamics and Monte-Carlo simulations, provide new insights into the structural impact of niobium oxide upon the short- and medium-range order of lithium silicate glasses.

2. Materials and methods

2.1. Glass preparation and characterization

Glasses in the pseudo-ternary compositional diagram $\text{Li}_2\text{O}-\text{Nb}_2\text{O}_5-\text{SiO}_2$ were synthesized via standard melt-cooling along two compositional lines, see Fig. 1 and Table 1; (1) gradual substitution of lithium disilicate glass (LS2) by niobium oxide, i.e., the series ($1-y$) $\text{Li}_2\text{Si}_2\text{O}_5-y\text{Nb}_2\text{O}_5$ ($y = 0, 0.02, 0.05$, and 0.10) and (2) gradual substitution of silica by a glass of composition $[(\text{Li}_2\text{O})_{1.4}-(\text{Nb}_2\text{O}_5)]$. The latter system features a fixed $\text{Li}_2\text{O}/\text{Nb}_2\text{O}_5$ ratio of 1.4 , which was previously found to be favorable for producing LiNbO_3 -containing glass-ceramics [29]. The glass formulations are $\frac{7x}{12(x+1)}(\text{Li}_2\text{O}) \frac{5x}{12(x+1)}(\text{Nb}_2\text{O}_5) \frac{1}{x+1}(\text{SiO}_2)$, where the compositional parameter x is defined by the ratio $([\text{Li}_2\text{O}] + [\text{Nb}_2\text{O}_5]) / [\text{SiO}_2]$ while keeping the ratio $[\text{Li}_2\text{O}] / [\text{Nb}_2\text{O}_5]$ constant at 1.4 . The x -values range from 1.0 to 3.5 , meaning that the SiO_2 content ranges from 50% for $x = 1.0$ to approximately 22% for $x = 3.5$.

For synthesis, raw materials Li_2CO_3 (Sigma Aldrich, 99.0%, and Shanghai Macklin Biochemical Co. Ltd., 99.99%), Nb_2O_5 (CBMM, Brazil, >99.99%), and SiO_2 (Zetasil 02, Brazil, 99.99%, and Shanghai Macklin Biochemical Co. Ltd., 99.99%) were dried in a muffle furnace at 120°C

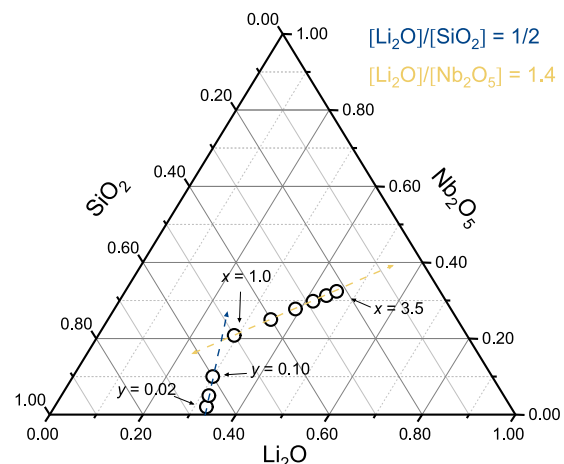


Fig. 1. Compositions of the synthesized glasses in mol% depicted in a pseudo-ternary diagram of the corresponding oxides. The blue and yellow dashed lines correspond to fixed $\text{Li}_2\text{O}/\text{SiO}_2$ and $\text{Li}_2\text{O}/\text{Nb}_2\text{O}_5$ ratios of $1/2$ and 1.4 , respectively.

for 12 h before mixing them in their respective molar ratios. After three rounds of homogenization in a Speedmixer™ (FlackTek) at 600 rpm for 3 min , the powdered mixtures were melted in a raising hearth furnace at 1400°C for 30 min in platinum crucibles. The melts were quickly cooled by casting them on a brass plate and splat-quenching them with a copper piston, resulting in visually homogeneous, colorless or slightly yellow-tinted, and bubble-free glasses, which were stored in a dry atmosphere.

For the $x = 1.5$ sample of the LNS series, the nominal Li, Si, and Nb contents were confirmed via inductively coupled plasma optical emission spectrometry (ICP-OES). The sample was digested through microwave-assisted dissolution in a mixture of nitric and hydrofluoric acid and then measured on a Thermo Scientific iCAP 7000 spectrometer. Measurements were repeated three times and averaged. For the LNS, $x = 1.5$ sample, the analytically determined Li_2O , Nb_2O_5 , and SiO_2 contents were 34.7 , 25.5 , and 39.8 mol\% , respectively, which agree with the nominal compositions within 0.5 mol\% . Glass densities, ρ , were determined using a precision scale (Mettler Toledo) according to the Archimedes principle in deionized H_2O at 298 K as the immersion liquid. Measurements were repeated five times and then averaged. Glass transition temperatures were determined on monolithic pieces of approximately $20 - 35\text{ mg}$ via Differential Scanning Calorimetry (DSC) on a Netzsch DSC 404 cell equipped with a TASC 414/3 controller at a heating rate of 10 K/min . Raman spectra were measured in the $200 - 1600\text{ cm}^{-1}$ range with an acquisition integration time of 100 s and 2 cycles using a LabRAM HR 800 Raman spectrophotometer (Horiba Jobin Yvon) equipped with a CCD detector (model DU420A-OE-325) and a He-Ne laser (632.81 nm).

2.2. Solid-State NMR

^{29}Si MAS NMR experiments were carried out at 5.64 T on an Agilent DD2 spectrometer (48.15 MHz Larmor frequency) in a 7.5 mm double resonance probe at a spinning frequency $v_{\text{MAS}} = 5.0\text{ kHz}$. 256 transients were collected at recycle delays ranging from 30 to 600 s , resulting in quantitatively representative spectra. Chemical shifts are reported with respect to TMS (0 ppm). ^7Li static and MAS NMR experiments were recorded at 5.64 T (94.20 MHz) in a 4.0 mm triple resonance probe at a MAS frequency of 14.0 kHz . All static measurements were conducted at -100°C to eliminate the effects of motional narrowing on the NMR spectra. 2048 transients were collected at recycle delays ranging from 0.5 to 15 s , depending on the sample and the temperature. ^7Li chemical shifts are reported with respect to 1 M LiCl solution (0 ppm). ^7Li satellite transition spectroscopy (SATRAS) [30] was performed at $v_{\text{MAS}} = 5.0\text{ kHz}$ for the analysis of the spinning sideband patterns arising from the

non-central (satellite) ${}^7\text{Li}$ Zeeman transitions. The ${}^7\text{Li}$ static and MAS NMR spectra were simulated, accounting for lineshapes due to first-order quadrupolar coupling and distributions of nuclear electric coupling constants (C_Q) according to the Czjzek model [31], implemented in the ssNake simulation program v1.5b [32]. The Czjzek model assumes a normal distribution of the electric field gradient (EFG) tensor components and results in a probability density function expressed in terms of C_Q and η_Q by

$$f(C_Q, \eta_Q) = \frac{C_Q^{d-1} \eta_Q}{\sqrt{2\pi}\sigma^d} \left(1 - \frac{\eta_Q^2}{9}\right) \exp\left\{-\frac{C_Q^2}{2\sigma^2} \left(1 + \frac{\eta_Q^2}{3}\right)\right\}, \quad (1)$$

where η_Q is the asymmetry parameter of the EFG tensor, d is the number of independent tensor components (typically 5, as in the present work), and σ is the standard deviation of the multidimensional Gaussian distribution. Simulations of the ${}^7\text{Li}$ NMR spectra in the presence of both electric quadrupolar and magnetic dipole-dipole interactions were performed using the SIMPSON package [33].

Static ${}^7\text{Li}$ spin-echo decay (SED) NMR experiments were conducted at -100°C (to remove contributions from dynamic relaxation to the echo decay) using the Hahn spin-echo sequence ($t_{\pi/2} - \tau_1 - t_\pi - \tau_1$) as described in detail elsewhere [34]. In order to reduce radio frequency amplitude gradients, only the center third of the used 4.0 mm rotors was filled with sample. A nutation frequency of 4.0 kHz, as measured on a 0.1 M solution of LiCl, proved sufficiently low to provide the required selective CT excitation in agreement with prior numerical SIMPSON simulations. Decay curves were modeled as Gaussians, which proved valid for multi-spin systems of spin $1/2$ nuclei [35] and valid for multi-spin systems of quadrupolar nuclei at sufficiently short dipolar mixing times [36] according to

$$\ln\left(\frac{I(2\tau_1)}{I(0)}\right) = -\frac{M_{2E(\text{Li-Li})}}{2} (2\tau_1)^2. \quad (2)$$

For $\text{Li}_2\text{Si}_2\text{O}_5$ and the output of the MD and MC simulations, second-moment values were calculated via the van-Vleck equation [37]

$$M_2 = f\left(\frac{\mu_0}{4\pi}\right)^2 \gamma_{\text{Li}}^4 \hbar^2 \frac{1}{N_{\text{Li}}} \sum_{i \neq j} \frac{1}{r_{ij}^6}, \quad (3)$$

where the numerical prefactor f is 9/4 for ${}^7\text{Li}$ with $I = 3/2$ in the absence of quadrupolar coupling and 0.9562 in the presence of quadrupolar coupling and selective excitation of the central Zeeman transition [38]. The second moment measured under these latter conditions will be denoted $M_{2E(\text{Li-Li})}$ in the following. For glasses, an average over N_{Li} nuclei is usually calculated from MD output.

${}^7\text{Li}$ - ${}^{93}\text{Nb}$ dipolar recoupling experiments were performed with the Rotational-Echo Saturation-Pulse Double-Resonance (RESPDOR) sequence [39], which was recently modified by us employing wideband uniform rate with smooth truncation (WURST) pulses [40] for saturation (W-RESPDOR) [41] at 14.10 T and $v_{\text{MAS}} = 20.0$ kHz in a 2.5 mm triple-resonance probe. ${}^7\text{Li}$ excitation and refocusing pulses were 4.0 and 8.0 μs in duration ($v_{\text{rf}} = 30.0$ kHz). A suitable WURST saturation pulse for the ${}^{93}\text{Nb}$ spin-system was found through numerical simulations (using the SIMPSON package [33]) with 8 rotor-cycles duration (400 μs), a shape parameter of $N = 80$, and a sweep width of 450 kHz at the highest possible experimental nutation frequency of 53.0 kHz (< 10% power reflection). The experimental W-RESPDOR curves were analyzed through fits to the data in the initial dipolar evolution regime ($\Delta S/S_0 \leq 0.2$) using the theoretical saturation-based recoupling curve [39,42]

$$\frac{\Delta S}{S_0} (\text{random}) = \frac{1}{2S+1} \left\{ 2S - \frac{\pi\sqrt{2}}{4(2S+1)} \sum_{k=1}^{2S} [4S - 2(k-1)] J_{\frac{1}{4}}(k\sqrt{2}\lambda) J_{-\frac{1}{4}}(k\sqrt{2}\lambda) \right\}, \quad (4)$$

which represents the analytical approximation of the dephasing curve

for a two-spin system. Here S is the spin quantum number of the non-observed spin (in this case, $S = 9/2$ for ${}^{93}\text{Nb}$), $\lambda = Dn\tau_r$ is a dimensionless parameter containing the dipolar coupling constant D and the dipolar mixing time $n\tau_r$, (product of the number of rotor cycles and the duration of a rotor cycle) and the terms $J_{\pm\frac{1}{4}}$ are Bessel functions of the first kind. We then derived, in analogy to the analytical approximation of the REDOR experiment of multi-spin systems [43], the first and second-order approximation of the theoretical saturation-based recoupling curve (see Section S2 of the Supporting Information section for the derivation)

$$\frac{\Delta S}{S_0} (\text{random}) \approx \frac{2}{3\pi^2} M_{2(\text{Li-Nb})}(n\tau_r)^2 + \frac{8S^3 - 16S^2 - 7S + 1}{21\pi^4 S(S+1)^2} M_2^2(n\tau_r)^4, \quad (5)$$

which implies, as an approximation, a dephasing independent of the geometry of a multi-spin system at sufficiently short dipolar mixing times. Here, $M_{2(\text{Li-Nb})}$ is the heteronuclear dipolar second moment. This value can be compared with the theoretical van Vleck value, calculated for the heteronuclear case via:

$$M_{2(\text{Li-Nb})} = \frac{33}{5} \left(\frac{\mu_0}{4\pi}\right)^2 \gamma_{\text{Nb}}^2 \gamma_{\text{Li}}^2 \hbar^2 \frac{1}{N_{\text{Li}}} \sum_{i=1}^{N_{\text{Li}}} \sum_{j=1}^{N_{\text{Nb}}} \frac{1}{r_{\text{Li-Nb}}^6} \quad (6)$$

In this expression, γ_{Nb} and γ_{Li} are the gyromagnetic ratios of the observed nucleus ${}^7\text{Li}$ and the recoupled spin-9/2 nucleus ${}^{93}\text{Nb}$. To calculate the expected $M_{2(\text{Li-Nb})}$ value from the simulation output, for each a sum over all the inverse sixth powers of the internuclear distances $r_{\text{Li-Nb}}$ is averaged for a sufficiently large number of ${}^7\text{Li}$ nuclei.

For the ${}^7\text{Li}$ - ${}^{93}\text{Nb}$ two-spin interaction, we have also numerically tested the dependence of the dephasing behavior on the relative orientations (β -angle) of their dipolar vector and the principal axis of the ${}^{93}\text{Nb}$ EFG tensor (see Fig. S1 in the Supporting Information). Simulations considering Li-Nb distances of 2.24 and 3.0 Å reveal β -angle dependent variations in the second moment of about 15% and 4%, respectively, corresponding to distance uncertainties of 0.1 and 0.05 Å. While isolated two-spin interactions are usually not encountered in our glasses, except possibly for the case of the 0.98LS2-0.02Nb₂O₅ sample, the simulations done here correspond to the currently best possible effort of estimating potential systematic errors encountered with the data analysis and interpretation.

${}^{93}\text{Nb}$ MAS NMR experiments were conducted at 14.10 T (146.80 MHz Larmor frequency) in a 1.3 mm double-resonance probe at a MAS rate of 60.0 kHz and a nutation frequency of $v_{\text{rf}} = 150$ kHz. For the direct polarization (single-pulse) and rotor-synchronous Hahn-Echo spectra, excitation pulse lengths of 0.2 μs and 0.6 μs were used at a recycle delay of 0.1 s. To minimize coil ringing effects, spectra were acquired after 4 rotor cycles. Spectra were fitted according to the Czjzek model (Eq. (1)). Chemical shifts were referenced against a saturated solution of NbCl₅ in acetonitrile (MeCN), using solid LiNbO₃ ($\delta_{\text{iso}} = 1004$ ppm) as a secondary standard.

2.3. Molecular dynamics and Monte Carlo simulations

The LAMMPS software package [44,45] was utilized for molecular dynamics (MD) simulations, with the rigid body potentials reported by Sun et al. [46]. These potentials consist of (i) a long-range Coulomb potential term, (ii) a short-range Buckingham term, and (iii) a dispersion interaction term, as shown below

$$(r) = -\frac{z_i z_j e^2}{r} + A_{ij} \exp\left(-\frac{r}{\rho_{ij}}\right) - \frac{C_{ij}}{r^6}, \quad (7)$$

considering interactions between Li-O, Si-O, Nb-O, and O-O atomic pairs. An additional correction term used by Sun et al. for short-range repulsion to prevent the system from collapsing when interatomic distances become very small during the simulation was not considered in the present work. We conclude that the relatively slower heating and

cooling rates employed here were sufficient to avoid the collapse of the system. Table S1 summarizes the simulation potential parameters used.

Long-range Coulomb interactions were assessed using Ewald summation with a force precision of 10^{-5} and a 12 Å cutoff. The velocity Verlet algorithm [47] was used to integrate Newton's equations of motion with a simulation timestep of 1 fs. Temperature and pressure were regulated using a Nosé–Hoover thermostat and barostat every 100 steps [48,49]. Periodic boundary conditions were applied on the three axes. Ensembles of about 10,000 atoms were randomly generated in a cubic simulation box, reproducing the compositions and experimental densities. The structure was first minimized for energy, then heated from 300 to 5000 K at a rate of 100 K ps⁻¹ using an NVT ensemble. The samples were held at the fusion temperature of 5000 K for 100 ps, then quenched to 300 K at a rate of 1 K ps⁻¹ under NVT conditions. The samples were thermalized at 300 K for 100 ps under the NVT ensemble condition, followed by another 100 ps under the NPT ensemble condition. An in-house software code was employed to analyze the data, calculating RDFs, M_2 values, and other relevant parameters. Also, Monte-Carlo (MC) simulations were performed by generating boxes with periodic boundary conditions populated randomly with Li and Nb atoms at the nominal concentrations based on experimental densities, using variable cutoff lengths for Li-Li, Li-Nb, and Nb-Nb distances. The M_{2E} _(Li-Li) and M_{2E} _(Li-Nb) values were then calculated from the output generated and compared with the experimental values.

For the calculation of M_{2E} _(Li-Nb) by MC simulations, we generated random atoms in a box with periodic conditions at the nominal Li and Nb concentrations (see Table 1) subject to constraints of Li-Li, Li-Nb, and Nb-Nb cutoffs, which are of 2.05, 3.30, and 3.55 Å, respectively, based on crystalline materials. Under these conditions, generating boxes for LS2 glass was only possible for $y = 0.02$, $y = 0.05$, $y = 0.1$, and $x = 1.0$. For the samples $x = 1.5$ to $x = 3.5$, it was impossible to generate random boxes under the above cutoff constraints. However, it is possible to generate independent random boxes for just Li or Nb. In the case of a pure Li-ion-containing box, with a 2.05 Å Li-Li cutoff, it is possible to generate atoms up to a concentration of 130 kmol/m³, which amounts to ~50% of the highest possible value for an FCC structure. Similarly, in the case of a pure Nb-ion-containing box, under an Nb-Nb cutoff of 3.55 Å, we get a maximum Nb concentration of 25 kmol/m³, which is also about 50% of the FCC structure. This indicates that there might be Li-Li and Nb-Nb clustering in samples $x = 1.5$ to 3.5 if they obey the same cutoffs as in the crystalline systems.

3. Results, data analysis, and interpretation

3.1. Glass characterization

The densities, molar volumes, and glass transition temperatures of the samples under study are listed in Table 1. The molar volumes observed for both systems increase as a function of x and y . This can be understood in terms of the large size of the niobium oxide polyhedra. The observed increase in T_g upon the successive substitution of lithium

disilicate by niobium oxide indicates an increase in the degree of polymerization as a function of y . For the LNS glass series, with the increase in the ratio $x = ([\text{Li}_2\text{O}]_{1.4+} [\text{Nb}_2\text{O}_5])/[\text{SiO}_2]$, the opposite trend is observed, consistent with a gradual decrease of the degree of network polymerization with increasing x . These predictions are borne out well by the ²⁹Si MAS-NMR results, to be discussed below. We note, however, that the T_g values observed in the LNS system are higher than expected based merely on the silicon speciation. We attribute this fact to the overall higher concentration of the Nb₂O₅ component, which will also contribute to bridging oxygen density and, hence, thermal stability via the formation of Nb-O-Nb linkages. Thus, a direct comparison of the two glass systems is only possible with respect to the compositional trends, not the absolute values of T_g .

3.2. Raman scattering

Fig. 2 shows the Raman spectra for the glasses under study. For LS2 glass, characteristic vibrational modes are observed corresponding to Si⁴ (470, 1030, and 1120 cm⁻¹), Si³ (580, 1080, and 1120 cm⁻¹), and Si² groups (665 and 950 cm⁻¹) [19,50]. These bands are already overshadowed in the glass with the smallest (2%) Nb₂O₅ content by the intense bands stemming from the highly polarizable Nb-O bonds. For the LS2-based glasses, an additional strong band can be seen at about 850 cm⁻¹ (c.f. region C in Fig. 2). For several Nb₂O₅-containing glasses, this frequency region was previously attributed to vibrational modes of NbO₆ octahedra with moderate to strong distortion, such as those sharing a corner with at least one other NbO₆ octahedron, with heteroatoms X in Nb-O-X linkages, and octahedra bearing non-bridging oxygen atoms [15–18,21,51]. This attribution is based on a systematic study of mixed alkali silicate glasses under variation of composition and correlation of Kerr coefficients with Raman spectra after the heat treatment of the glasses [18].

According to Fukumi et al., the scattering band near 800–950 cm⁻¹ (region C in Fig. 2) up-shifts with increasing octahedra distortion and an increasing number of non-bridging oxygen atoms. Here such a distortion could be imagined if Nb in octahedral coordination was found to exhibit Nb-O-Si linkages with Si tetrahedra or for edge-sharing NbO₆ octahedra as in the case of AlNbO₄ [21].

For silicate glasses containing K₂O and Nb₂O₅, the relative intensity of this band increases with decreasing SiO₂ content, given a fixed K₂O/Nb₂O₅ ratio similar to the Li₂O-containing glasses reported here. As y increases in the (1- y)LS2- y Nb₂O₅ system, the main band near 850 cm⁻¹ is accompanied by a shoulder near 800 cm⁻¹, which can be assigned to the Nb-O stretching modes of NbO₆ units involved in Nb-O-Nb linkages. The growth of this shoulder with increasing Nb content suggests a progressive linking (clustering) of corner-shared, less distorted NbO₆ octahedra [21]. For $y = 0.1$, another shoulder in the 650–750 cm⁻¹ region is observable (region A), which Fukumi et al. attributed to NbO₆ units with low distortion and not bearing NBOs [16].

The Raman spectra of the LNS glasses are similar to those presented previously in the literature for glasses of similar compositions [52,53].

Table 1

Nominal compositions, densities ρ , and glass transition temperatures T_g of the (1- y)LS2- y Nb₂O₅ and LNS glasses.

y	[Li ₂ O] / mol%	[Li ₂ O] / kmol/m ³	[Nb ₂ O ₅] / mol%	[Nb ₂ O ₅] / kmol/m ³	[SiO ₂] / mol%	ρ / g/cm ³ (5·10 ⁻⁴)	V_M / cm ³ /mol (± 0.005)	T_g / °C (± 2)
0	33.3	30.9	0	0.0	66.7	2.3211	21.548	456
0.02	32.7	29.5	2	1.8	65.3	2.4513	22.164	477
0.05	31.7	27.4	5	4.3	63.3	2.6280	23.137	502
0.10	30.0	24.2	10.0	8.1	60.0	2.8930	24.748	539
x								
1.0	29.2	20.3	20.8	14.5	50.0	3.2803	28.694	566
1.5	35.0	24.1	25.0	17.2	40.0	3.4779	29.024	556
2.0	38.9	26.5	27.8	18.9	33.3	3.5928	29.360	548
2.5	41.7	28.1	29.8	20.1	28.6	3.6646	29.668	541
3.0	43.8	29.2	31.3	20.9	25.0	3.7150	29.921	535
3.5	45.4	30.0	32.4	21.4	22.2	3.7400	30.228	531

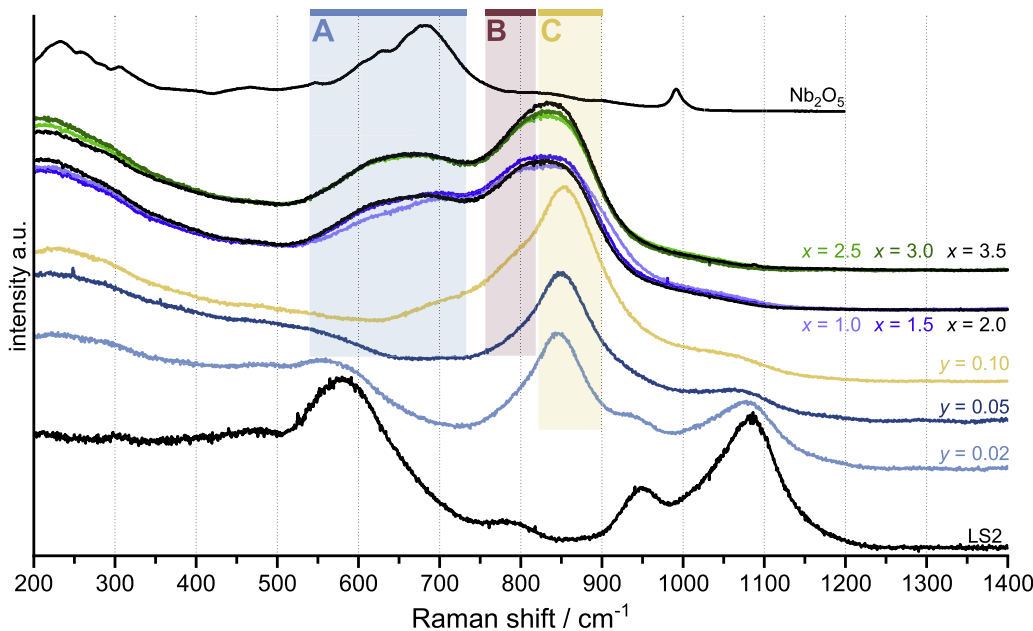


Fig. 2. Raman spectra of LS2 glass, $(1-y)\text{LS2}-y\text{Nb}_2\text{O}_5$ glasses with $y = 2, 5$, and $10\text{mol}\%$ Nb_2O_5 and LNS glasses. The most prominent spectral features corresponding to Nb-O vibrational modes have been highlighted. See the text for the definition of regions A, B, and C.

and differ substantially from those of the $(1-y)\text{LS2}-y\text{Nb}_2\text{O}_5$ system. Encompassing the regions C and B, the broad band centered near 820 cm^{-1} may be attributed to a superposition of the features at 850 and 800 cm^{-1} discussed above, with the latter being considerably more intense in the LNS glasses. Here we note that the $x = 1.0$ sample has a pronounced shoulder near 920 cm^{-1} , which in light of its low ratio of non-bridging oxygen atoms (NBOs) per Nb (see discussion of ^{29}Si MAS NMR data below), suggests that it may arise from linkages to Si rather than from NBOs. More importantly, the spectra of all the LNS glasses show intense scattering in region A ($650 - 750\text{ cm}^{-1}$), almost independent of composition.

In fact, the spectral region (c.f. region A in Fig. 2) is very similar to that observed for crystalline Nb_2O_5 (see Fig. 2, top) and LiNbO_3 [54]. The feature near 600 cm^{-1} was previously attributed to NbO_6 octahedra within a three-dimensional network and is also observed for Nb in perovskite-like environments. For increasing Nb contents, the center of gravity of this broad band is shifted to lower wavenumbers. In a related potassium niobium germanate glass system [20], this shift was attributed to a change in the connectivity of $\text{Nb}(\text{OGe})_{6-z}(\text{ONb})_z$ units, for which the number of ONb neighbors z increases with increasing Nb content, as suggested by Raman [20] and ^{93}Nb solid-state NMR experiments [25]. Based on the present ^{93}Nb MAS NMR results (see below), and in light of decreasing Si contents with increasing x , we make a similar attribution of the scattering peaks in spectral region A to less distorted NbO_6 units with differing amounts of Si and Nb in its second-coordination sphere. The absence of these spectral features in the LS2 glasses containing 2 and 5% Nb_2O_5 provides some evidence that, in these samples, the NbO_6 units still avoid clustering and are instead integrated into the silicate network, i.e., they are present as Nb(OSi)_6 units, as previously hypothesized [15]. Overall, the subtle changes of the Raman spectra along the LNS glass series, compared to the spectra of the LS2 series, corroborate previous findings that the Nb species distribution is mostly dependent on the $\text{Li}_2\text{O}/\text{Nb}_2\text{O}_5$ ratio, which is fixed in the present case [16]. Studies on crystalline materials show that principally heteropoly niobates like $[\text{Nb}_6\text{O}_{19}]^{8-}$ are not very well stabilized by the small Li^+ cation, and due to this low association tendency, the formation of these species in Li-containing glasses may not take place [55].

3.3. ^{29}Si MAS NMR

Fig. 3 shows the ^{29}Si MAS NMR spectra obtained on the two studied glass series. Broad, rather featureless lineshapes are obtained, which can be deconvoluted into multiple contributions from the Gaussian components representing the various Si^n units. For the LS2-based glasses, the deconvolution model applied to lithium disilicate glass ($y = 0$) can serve as a useful starting point with three Gaussians, centered at -79.4 , -90.6 , and -104.1 ppm, corresponding to Si^2 (11%), Si^3 (78%), and Si^{4a} (11%) units [56]. Successive replacement of lithium disilicate by Nb_2O_5 with increasing y (Fig. 3, left) produces only subtle changes in the center of gravity, δ_{CG} (see Table 2). However, satisfactory lineshape fitting requires an additional lineshape component near -98 ppm, referred to as Si^{4b} . As the contribution of this component increases with Nb_2O_5 content, we tentatively assign it to Si^4 units involved in three Si-O-Si linkages and one Si-O-Nb linkage. Such a Si unit was previously observed in binary sol-gel derived amorphous $\text{Nb}_2\text{O}_5-\text{SiO}_2$ materials [26], and its existence is compatible with the Raman band near 850 cm^{-1} . With the inclusion of this additional component, excellent lineshape deconvolutions are obtained for both the LS2-based and the LNS glass series, see Table 2.

In these fits, an additional lineshape component appears for samples with $x = 3.0$ and 3.5 , corresponding to Si^1 units while keeping the positions and widths of the remaining components mostly invariant (see also Table 2). While, of course, many other deconvolution models may be applicable, the present one takes into account charge-balance considerations. It also carefully accounts for specific chemical shift regions of Si^n units, minimizes the variation of signal positions and widths, and produces monotonic composition-dependent parameter trends. Attempts to obtain direct evidence for Si-O-Nb linkages using $^{29}\text{Si}\{^{93}\text{Nb}\}$ REAPDOR and recently developed WURST-RESPDOR double resonance NMR methods [41] were unsuccessful due to the low signal-to-noise ratio for ^{29}Si detection.

Overall, the ^{29}Si MAS NMR spectra reveal that the degree of silicate network polymerization increases moderately from $\langle n_{\text{Si}} \rangle = 3.00$ to $\langle n_{\text{Si}} \rangle = 3.23$ in the LS2 system and decreases significantly in the LNS system, from $\langle n_{\text{Si}} \rangle = 3.31$ in the $x = 1$ glass to $\langle n_{\text{Si}} \rangle = 2.10$ in the $x = 3.5$ glass. As discussed further below, these changes are different from those expected merely upon consideration of the $\text{Li}_2\text{O}/\text{SiO}_2$ ratios indicating

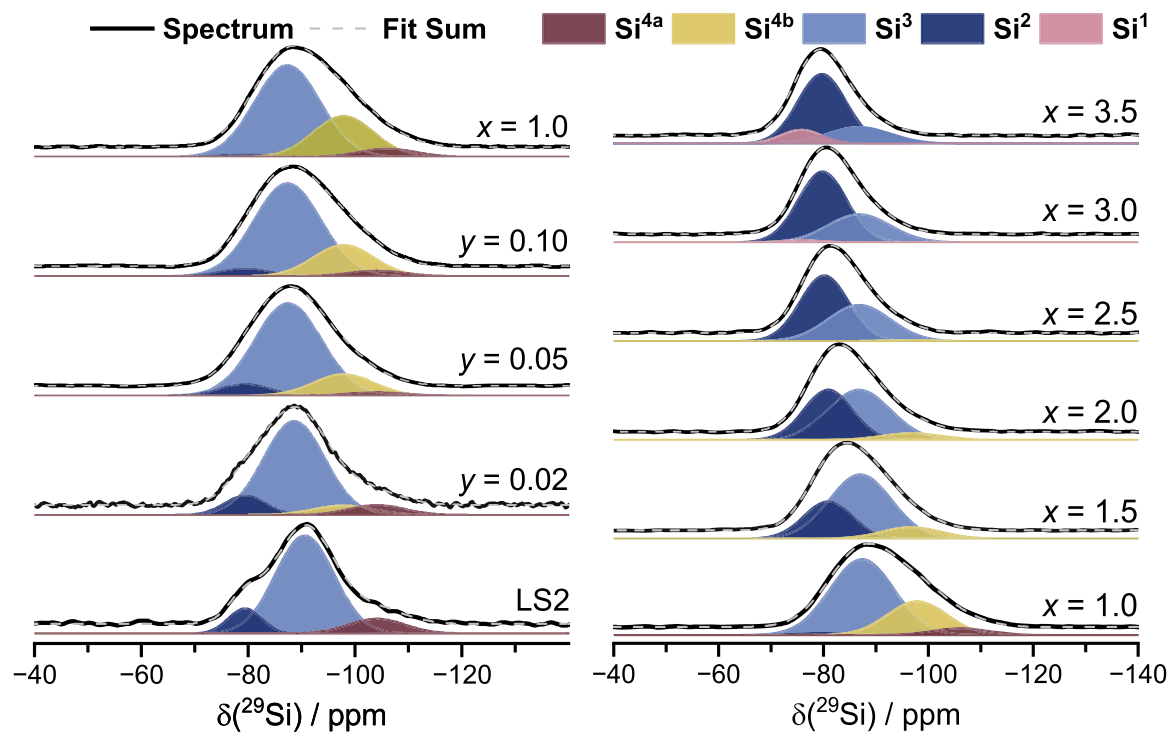


Fig. 3. ^{29}Si MAS NMR spectra of LNS glasses under study: Left: lithium disilicate based glasses (LS2) containing Nb_2O_5 according to the designated labels. Right: LNS glasses with compositions $x = (1.4\text{Li}_2\text{O} + \text{Nb}_2\text{O}_5) / \text{SiO}_2$.

Table 2

Center of gravity, δ_{CG} , of the ^{29}Si MAS NMR lineshape and isotropic chemical shifts, δ_{iso} , full widths at half maximum, FWHM, area fractions, f , and network polymerization $\langle n_{\text{Si}} \rangle$, extracted from lineshape simulations.

(1-y)LS2-yNb ₂ O ₅				Composition x						
y	0	0.02	0.05	0.10	1.0	1.5	2.0	2.5	3.0	3.5
$\delta_{\text{CG}} / \text{ppm}$	-90.4	-89.4	-88.9	-90.0	-91.2	-86.2	-85.1	-82.9	-82.1	-80.6
(± 0.2)										
$\delta_{\text{iso}} / \text{ppm}$										
(± 0.2)										
Si ¹	-	-	-	-	-	-	-	-	-75.7	-75.7
Si ²	-79.4	-79.4	-79.4	-79.4	-79.4	-80.9	-80.9	-80.2	-79.8	-79.7
Si ³	-90.6	-88.6	-87.5	-87.4	-87.4	-87.0	-86.8	-86.8	-86.8	-86.8
Si ^{4b}	-	-97.9	-97.9	-97.9	-97.9	-96.8	-96.8	-96.8	-	-
Si ^{4a}	-104.1	-104.1	-104.1	-104.1	-106.1	-	-	-	-	-
FWHM / ppm										
(± 0.5)										
Si ¹	-	-	-	-	-	-	-	-	9.1	9.1
Si ²	7.4	9.1	10.9	10.9	10.9	9.1	9.1	10.9	10.9	10.9
Si ³	13.0	13.6	14.8	14.9	14.5	14.1	13.6	13.6	14.1	14.1
Si ^{4b}	-	13.3	13.3	13.3	13.3	13.3	13.3	13.3	-	-
Si ^{4a}	12.5	12.5	12.5	12.5	12.5	-	-	-	-	-
$f / \% (\pm 2)$										
Si ¹	-	-	-	-	-	-	-	-	2	11
Si ²	11	11	7	2	1	28	41	58	65	68
Si ³	78	75	75	73	67	62	52	41	33	21
Si ^{4b}	-	7	16	21	27	11	7	1	-	-
Si ^{4a}	11	7	2	4	5	-	-	-	-	-
$\langle n_{\text{Si}} \rangle$	3.00	3.03	3.11	3.23	3.31	2.86	2.66	2.43	2.31	2.10

that the intermediate oxide Nb_2O_5 also participates in the interaction with the network modifier inventory. In order to assess the effects of the Nb_2O_5 species on the studied glasses, charge balance considerations are helpful. Here, we will assume that $4-n \text{Li}^+$ ions exclusively balance the charges on the Si^n species. Any Li^+ species above this amount must be associated with anionic niobium species, compensating their charges. The number of NBOs according to the silicon Si^n species inventory was calculated based on the fractional areas shown in Table 2 and compared to the number of NBOs introduced by Li_2O , see Table 3.

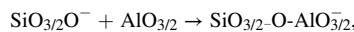
For the Nb-containing LS2-based samples, the proposed deconvolution model reveals that the total amount of NBOs introduced by Li_2O in the silicon network is lower than expected from the Li/Si ratio, suggesting that part of the Li_2O is used to charge-balance anionic niobium species. For the LNS glasses, the ratios k of the NBOs produced by Li_2O , which are unaccounted for by the Si^n units ([NBO(residual)]), to the number of Nb atoms are similar, and comparable (near 0.66) to those observed for the LS2 system. The $x = 1.5$ sample presents the only exception; see the last column of Table 3. The observed lower-than-unity

Table 3

Concentration of non-bridging oxygen (NBO) atoms in each glass according to the Siⁿ distribution obtained from the ²⁹Si MAS NMR spectral deconvolution and introduced by the network modifier Li₂O compared to the concentration of Nb atoms.

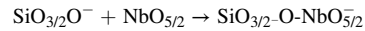
y	[NBO] (Si ⁿ) / (± 2) mol %	[NBO] Li ⁺ / mol %	[NBO] (residual) / mol%	[Nb] / mol% / [Nb] (residual) / mol% (± 0.15)	k = [NBO] (residual) / [Nb] (± 0.15)
0	66.7	66.7	0.00	—	—
2	62.1	65.3	3.3	4	0.82 (± 0.5)
5	56.4	63.3	7.0	10	0.70
10	46.2	60.0	13.8	20	0.69
x					
1.0	34.5	58.3	23.8	41.7	0.57
1.5	47.2	70.0	22.8	50	0.46
2.0	44.7	77.8	33.1	55.6	0.60
2.5	44.9	83.3	38.5	59.5	0.65
3.0	42.3	87.5	45.3	62.5	0.72
3.5	42.2	90.8	48.5	64.8	0.75

values suggest that, in all samples, not all of the NbO₆ octahedra are charge compensated or carry NBOs, but there must be a distribution of NbO₆ species, which also varies slightly with the glass composition. This finding is in agreement with our hypothesis based on the observed vibrational bands in the Raman spectra and corroborates the suggested deconvolution model. The interpretation of the k value of 0.7 is tentative at present. The structural effect of Al₂O₃, another intermediate oxide, upon alkali silicate glasses is well documented: here, one NBO is eliminated for each Al³⁺ ion added, leading to the formation of an anionic AlO₄/2 unit attracting one network modifier ion for charge compensation, corresponding to a k-value of unity, the net formal melt reaction being described as



with the negative charge formally located on the four-coordinated Al atom. In the case of Nb₂O₅, a similar mechanism can be envisioned, forming a corner-sharing anionic [NbO_{6/2}]⁻ unit, attracting one

network modifier ion for charge compensation:



Again, k = 1 would be expected if this process went to completion. The sub-unity value of k observed in the present case may indicate that part of the niobium species is incorporated without attracting charge, possibly due to the formation of clusters involving edge-sharing between NbO₆ octahedra.

3.4. ⁹³Nb MAS-NMR

To obtain more direct information on the local environments of the Nb units, ⁹³Nb MAS NMR experiments were carried out. MAS NMR spectra of Nb₂O₅ and LiNbO₃ are shown in Fig. 4 for comparison. Despite the relatively high Larmor frequency of 146.8 MHz, single-pulse acquisition led to spurious coil-ringing signals, significantly distorting the obtained NMR spectra (data not shown). Therefore, fast-spinning rotor-synchronized ⁹³Nb Hahn-echo MAS NMR spectra were recorded (see Fig. 5). These experiments employed interpulse delays equivalent to two rotor periods, led to signals free of coil-ringing, and thus, did not require first-order phase correction. It was possible to obtain identical spectra from ⁹³Nb direct polarization (one pulse) and one rotor-cycle Hahn-echo synchronized MAS NMR experiments after appropriate first-order phase correction.

The central-transition spectrum of LiNbO₃ (see inset Fig. 4) shows a lineshape influenced by quadrupolar interactions and can be successfully modeled by second-order perturbation theory. Simulation of the MAS powder pattern using ssNake yields C_Q = 21.9 MHz and η_Q = 0.06 at an isotropic chemical shift of -1003 ppm (see also Table 6) [57–59]. These values are close to those published in the literature [57]. The central transition (CT) is flanked by a set of spinning sidebands, arising from the modulation of the eight anisotropically broadened non-central satellite m_l ↔ m_l±1 transitions. The spectrum of crystalline Nb₂O₅ exhibits a similar, however, expectedly more complex CT lineshape, reflecting the numerous nonequivalent Nb sites in this compound [27, 60]. The lineshape can be satisfactorily fitted to a set of four distinct

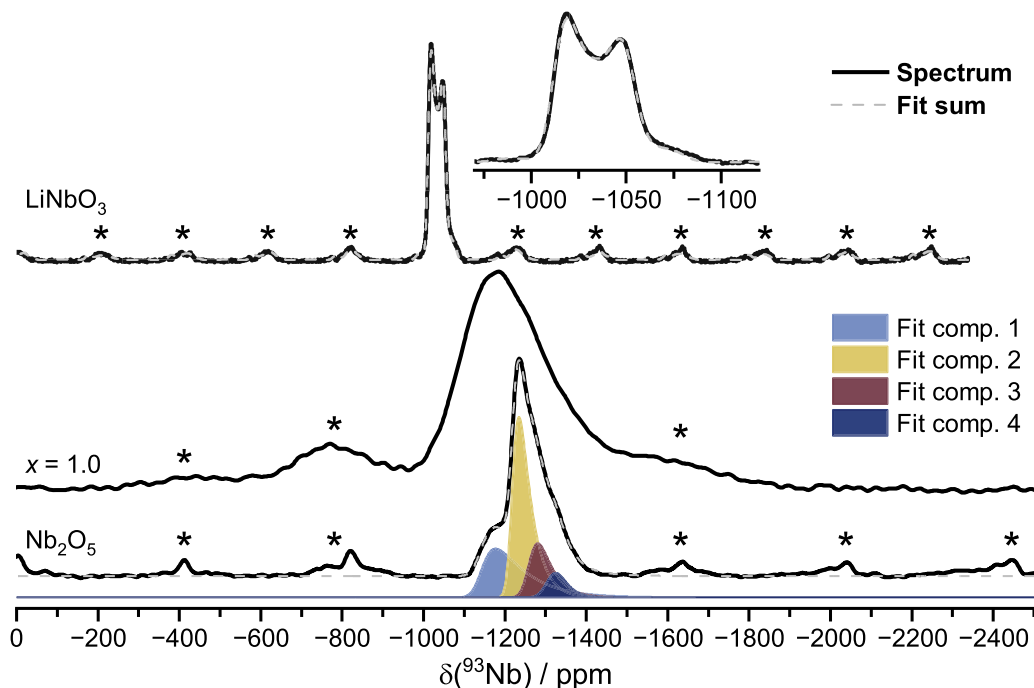


Fig. 4. ⁹³Nb MAS NMR spectra of LiNbO₃ (top), Nb₂O₅ (bottom), and rotor-synchronized ⁹³Nb Hahn-echo MAS NMR spectra (two rotor-cycles) of LNS glass with composition x = 1.0 (center). The gray dashed curves indicate lineshape simulations for LiNbO₃ and the sum of the fit components (colored curves) for Nb₂O₅. Asterisks indicate spinning sidebands.

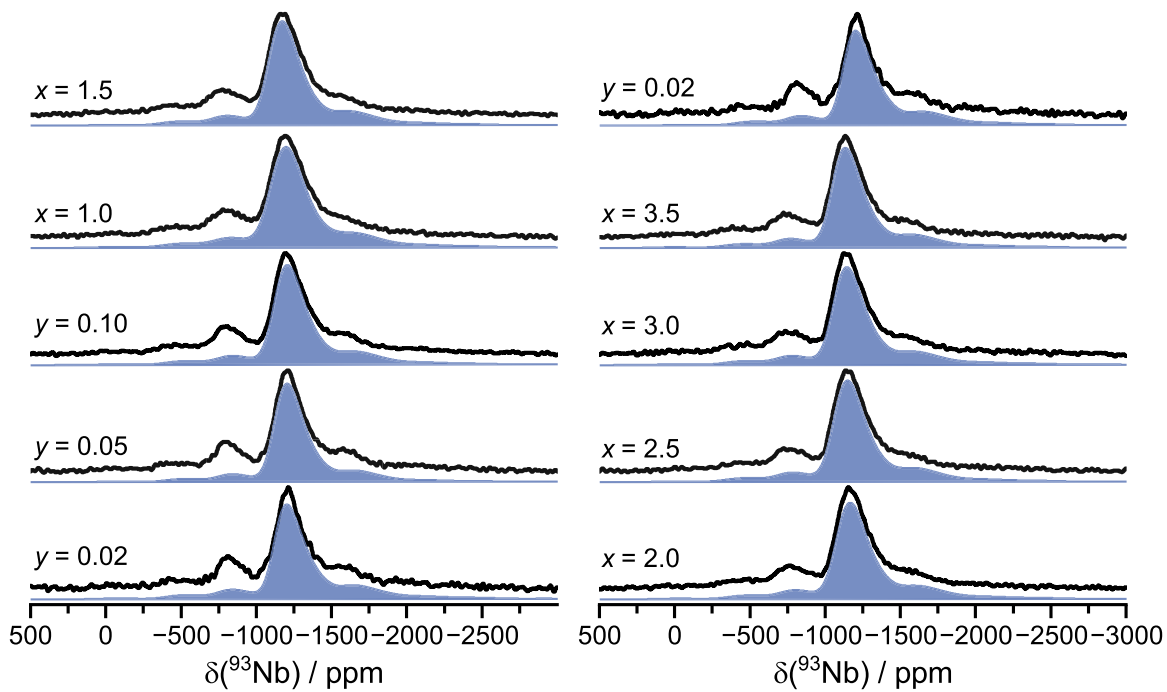


Fig. 5. ^{93}Nb rotor-synchronized MAS Hahn-echo spectra (black lines) after two rotor cycles for LS2-based glasses and the LNS glasses under study. Simulations (blue-shaded lines) are included based on a singular Czjzek distribution. Potential contributions of the ^{93}Nb chemical shift anisotropy were not considered in these simulations.

components, each reflecting the effects of a distribution (Czjzek model) of electric field gradients on the Zeeman frequencies as predicted by second-order perturbation theory. Fig. 4 shows the tentative simulation by a set of four distinct components, with isotropic chemical shifts ranging from about -1140 to -1305 ppm, and average magnitudes of the quadrupolar coupling constants of 18.9 to 33.7 MHz, all in agreement with pentavalent niobium in distorted six-coordination [57] (see also Table 4). The assignment of these peaks is still uncertain owing to the complex nature of the Nb_2O_5 crystal structure, featuring a unit cell containing 28 niobium atoms [61]. Additionally, the observable spinning sidebands are relatively narrow and well-defined. Evidently, the varying coordination symmetries of the off-centered NbO_6 ions, which are engaged in both corner- and edge-sharing [62,63], result in an effective distribution of EFGs, similar to the situation present in the glasses.

Table 4

^{93}Nb NMR parameters, isotropic chemical shift (δ_{iso}), the average magnitude of the quadrupole coupling constant ($|\bar{C}_Q|$), Czjzek distribution width of quadrupole coupling constants (σ), Gaussian line broadening (FWHM GB), and fractional areas f of the samples under study.

Composition	δ_{iso} / ppm (± 5)	$ \bar{C}_Q $ (σ) / MHz (± 2)	FWHM GB / ppm (± 5)	f / % (± 2)
Nb_2O_5				
Component 1	-1137	33.7 (16.9)	44	29
Component 2	-1216	21.1 (10.6)	26	46
Component 3	-1257	23.0 (11.6)	37	18
Component 4	-1305	18.9 (9.5)	42	7
LiNbO_3	-1003	$C_Q = 21.9 / \eta_Q = 0.06$	$13 (\pm 1)$	100
$y = 0.02$	-1117	49.3 (24.8)	136	100
$y = 0.05$	-1122	45.8 (23.0)	146	100
$y = 0.10$	-1120	47.5 (23.9)	152	100
$x = 1.0$	-1103	48.2 (24.4)	183	100
$x = 1.5$	-1084	44.1 (24.0)	156	100
$x = 2.0$	-1077	47.8 (24.0)	161	100
$x = 2.5$	-1060	47.8 (24.0)	160	100
$x = 3.0$	-1056	47.8 (24.0)	154	100
$x = 3.5$	-1048	47.4 (23.8)	148	100

The spectra of all the glasses show significantly wider and asymmetrically broadened central transitions flanked by a set of spinning sidebands. In this case, a simulation of the center band succeeds based on a singular Czjzek component (see Fig. 5), however, the spinning sidebands are not well accounted for in the model, indicating a significant contribution of the chemical shift anisotropy (CSA). Recent ^{93}Nb MAS NMR work on niobium germanate glasses [25] and phosphate glasses [6] reported much narrower and structured lines over the chemical shift range of about -1000 to -1500 ppm, indicating the presence of individual components with distinct chemical shifts. While the observed vibrational bands in the Raman spectra of the present glasses also show that there is a distribution of Nb species with different coordination geometries, the ^{93}Nb NMR spectra of the present glasses show only rather featureless lineshapes, which do not offer the necessary resolution to distinguish between multiple species. In order to further explore the presence of several individual resonance lines, ^{93}Nb 3QMAS NMR was performed, and the spectra are shown in Fig. S2 for the glasses $x = 1.0$ and 3.5 . Unfortunately, due to the short spin-spin relaxation times (T_2), the triple-quantum coherence decayed already for rather short evolution times and only a few points could be measured, resulting in rather poor signal-to-noise ratios limiting the resolution of these spectra. The spectra do not indicate any form of resolution into distinct signal components. Additional information on the speciation of many NMR active glass network forming elements can often be obtained through spectral editing experiments from double-resonance methods like REDOR, REAPDOR, or RESPDOR NMR. In the present case, ^{93}Nb observed double resonance experiments were unfortunately not feasible in our laboratory due to the lack of a double-resonance probe with access to the necessary high spinning frequencies (> 60 kHz).

The extracted isotropic chemical shifts lie between -1122 to -1048 ppm. They cover a region previously observed in other oxide glasses, where they have been typically assigned to NbO_6 polyhedra [6,22–28, 57]. For the LS2-based system, the isotropic chemical shifts are independent of y , which agrees with the compositional near-invariance observed in the Raman spectra. For the LNS glass system, the isotropic chemical shifts show a monotonic trend to increase by ca. 50 ppm over

the entire series; this relatively moderate evolution matches the subtle changes in the Raman spectra, suggesting a gradual change in the fraction of corner- versus edge-sharing NbO_6 octahedra. More specifically, the ^{93}Nb isotropic chemical shift for samples with $x > 2.5$ are comparable to those found in recently reported germanate glasses [25], where it was suggested that the second-coordination sphere around the NbO_6 units is dominated by other NbO_6 octahedra while for the glasses with lower Nb_2O_5 content, it is at least partially made up by GeO_4 tetrahedra. This attribution stands in agreement with the Raman data, which suggests an increased formation of a separate Nb-O-Nb connected network of NbO_6 units with increasing Nb_2O_5 content.

3.5. ^7Li MAS-NMR

Based on the above results, it is expected that the distribution of network modifier ions and their local environments may differ significantly between the investigated samples. Therefore, MAS-NMR of the ^7Li ($I = 3/2$) nuclei was conducted to elucidate the short-range ordering of the Li^+ ions. The results are summarized in Fig. 6. Similar to the situation encountered in previous ^7Li MAS-NMR studies of lithium silicate glasses [56,64,65], the spectra are dominated by an intense sharp resonance corresponding to the $m = \pm 1/2 \leftrightarrow m = \pm 3/2$ central transition, accompanied by a spinning sideband manifold, reflecting the effect of MAS on the anisotropically broadened lineshapes of the quadrupole-perturbed $m = \pm 1/2 \leftrightarrow m = \pm 3/2$ satellite transitions (SATRAS). As previously found [56], the intensity profile of this SATRAS manifold is affected by a distribution of quadrupolar coupling parameters, which can be simulated using the Czjzek model. The extracted interaction parameters are shown in Table 5.

The MAS-NMR spectra of all samples reveal CTs centered between -0.2 and 0.75 ppm with linewidths between 400 and 600 Hz (about 4 – 6 ppm). In the LS2-based system, the linewidths and chemical shifts decrease with increasing Nb_2O_5 content, whereas in the LNS system, a successive increase can be noted. The widths (σ -values) of the Czjzek

distributions, on the other hand, decrease monotonically with increasing y . A slight decrease is also noted in the LNS series; however, the variation is much less, and nearly constant values are reached for $x = 2.0$, $y = 0.02$.

Table 5

^7Li NMR parameters, isotropic chemical shift (δ_{iso}), average magnitude of the quadrupole coupling constant ($|\bar{C}_Q|$), Czjzek distribution width of quadrupolar coupling constants (σ), CT-NMR static NMR linewidth (FWHM), and homonuclear ^7Li – ^7Li dipolar second moments $M_{2E(\text{Li-Li})}$ from experiment and from MD simulation (see below) of the samples under study.

y	δ_{iso} / ppm (± 0.05)	FWHM GB / ppm (\pm 0.5)	$ \bar{C}_Q $ (σ) / kHz (± 5)	FWHM / kHz (\pm 0.5)	$M_{2E(\text{Li-Li})}$ / $10^6 \text{ rad}^2/\text{s}^2$ ($\pm 2.5 \times$ $10^5 \text{ rad}^2/\text{s}^2$)	$M_{2E(\text{Li-Li})}$ / $10^6 \text{ rad}^2/\text{s}^2$ ($\pm 10 \times$ $10^5 \text{ rad}^2/\text{s}^2$)
0	-0.20	5.5	187 (94)	7.16	99	170
0.02	-0.22	5.2	173 (87)	7.60	93	160
0.05	-0.23	4.9	174 (88)	7.30	89	146
0.10	-0.41	4.5	159 (80)	6.97	84	119
x						
1.0	-0.73	4.4	128 (65)	6.95	75	72
1.5	-0.70	5.1	125 (63)	7.79	76	85
2.0	-0.75	5.5	120 (61)	7.29	86	n.d.
2.5	-0.72	5.8	119 (60)	8.58	87	n.d.
3.0	-0.62	6.1	117 (59)	8.90	88	n.d.
3.5	-0.54	6.3	117 (59)	9.08	93	109

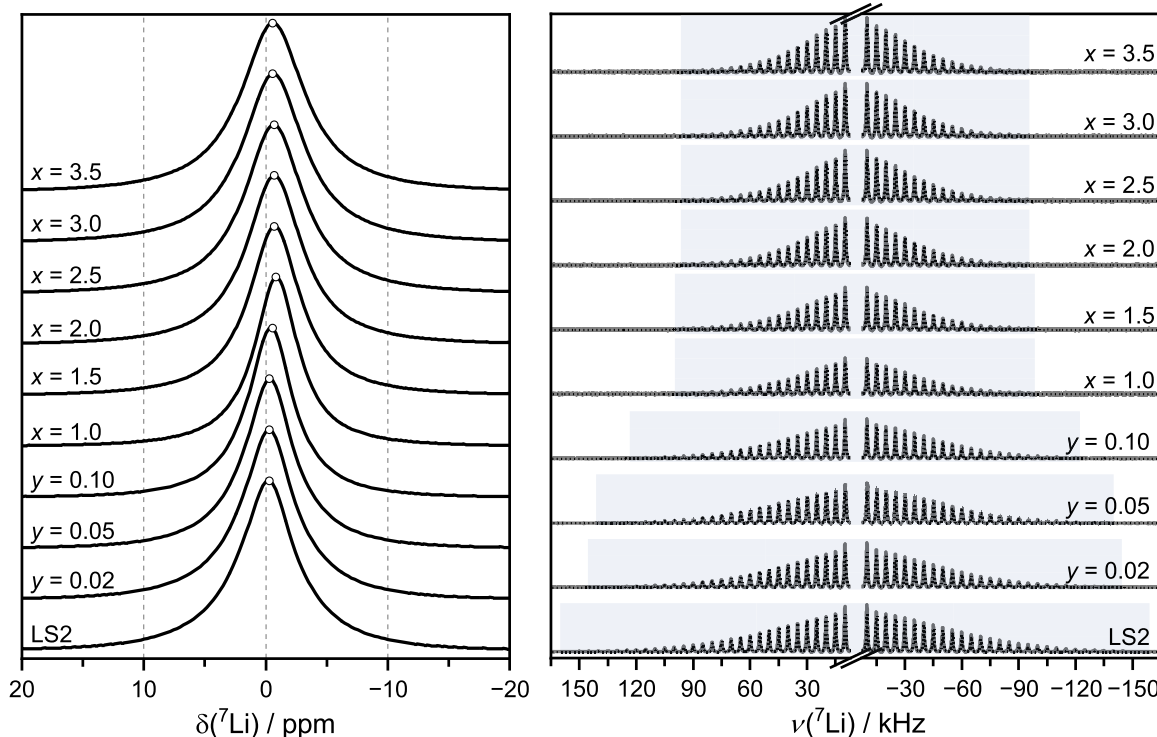


Fig. 6. Left: Centerband of ^7Li MAS NMR spectra of the glass samples under study. Circles indicate the maxima of the signals as a guide to the eye. Right: Whole ^7Li SATRAS NMR spectra, showing the full spinning-sideband patterns. Fits according to the Czjzek model are shown as dotted curves. The light-blue highlighted regions indicate the breadth for which spinning sidebands are distinguishable from the noise level.

Table 6

Experimental heteronuclear dipolar second moments, $M_{2(\text{Li-Nb})}$, obtained from fits to the data using Eqs. 4 (analytical) and 5 (parabola), and simulated values obtained from MD simulations.

y	$M_{2(\text{Li-Nb})}$ (analytical) / $10^6 \text{ rad}^2/\text{s}^2 (\pm 5\%)$	$M_{2(\text{Li-Nb})}$ (parabola) / $10^6 \text{ rad}^2/\text{s}^2 (\pm 5\%)$	$M_{2(\text{Li-Nb})}$ (MD) / $10^6 \text{ rad}^2/\text{s}^2 (\pm 5\%)$
LiNbO ₃ (sim.)	271.1 ($\pm 10\%$)	–	–
0.02	4.9	4.9	8.8
0.05	13.6	12.5	23.8
0.10	24.2	20.5	51.1
x			
1.0	38.2	29.2	106.1
1.5	39.9	30.1	122.5
2.5	46.7	33.7	n.d.
3.0	44.4	32.5	n.d.
3.5	47.2	34.0	152.3

indicating that the local EFG distribution may depend chiefly on the Li₂O/Nb₂O₅ ratio. The above observations can be attributed to changes in the Li-coordination environment, which are increasingly influenced by Nb with increasing y in the LS2-based system, whereas in the LNS system, the Li ions appear to adopt a nearly constant local environment, following minor initial structural changes near $x = 1.0$ to $x = 1.5$.

3.6. ${}^7\text{Li}$ static and dipolar NMR

Static ${}^7\text{Li}$ NMR spectra are shown in Fig. 7 (left). These spectra are dominated by the homonuclear dipolar interactions among the ${}^7\text{Li}$ nuclei and by heteronuclear dipolar interactions between ${}^7\text{Li}$ and ${}^{93}\text{Nb}$ nuclei. While for the LS2-based glasses, the linewidths are rather invariant within the experimental error, a significant increase can be observed for the LNS glasses with increasing x , as expected from the increasing Li₂O content. This increase can be attributed to increases in either the ${}^7\text{Li}$ - ${}^7\text{Li}$ or the ${}^7\text{Li}$ - ${}^{93}\text{Nb}$ dipolar interaction strengths or both. Unfortunately, from the static NMR spectra alone, quantitative information cannot be obtained as the homonuclear and heteronuclear coupling contributions to the static lineshapes cannot be separated.

To differentiate between these possibilities, we employed ${}^7\text{Li}$ spin echo decay spectroscopy, first introduced to lithium disilicate glasses in reference [34] to selectively measure the average dipolar coupling strength in the form of the homonuclear ${}^7\text{Li}$ – ${}^7\text{Li}$ second moment M_{2E} (Li-Li), see Fig. 7 (right) and Table 5. It can be observed that the value for LS2 glass of $99 \times 10^6 \text{ rad}^2/\text{s}^2$ decreases with decreasing Li₂O content as a function of y . Interestingly, while the total Li₂O content is higher for the LNS glass series with $x > 1.0$, the ${}^7\text{Li}$ second-moments are significantly lower, reflecting the competition of Nb and Si for network modifiers. In the LNS series, the $M_{2E(\text{Li-Li})}$ values show a tendency to increase with increasing x , and for the sample with $x = 3.5$, the $M_{2E(\text{Li-Li})}$ value is very close to that in LS2 glass. Again, the compositional trend of the second moment is correlated to the isotropic chemical shifts.

To selectively measure the network modifier – network former interaction between ${}^7\text{Li}$ and ${}^{93}\text{Nb}$, we have exploited rotational-echo saturation-pulse double-resonance NMR (RESPDOR) employing WURST pulses for saturation (W-RESPDOR), capable of recoupling the dipolar interaction between spin pairs in which large shielding anisotropies or strong quadrupolar interactions contribute to the Hamiltonian [41]. While RESPDOR has been successfully applied to several nuclear spin pairs in different materials [41], it has been mostly used for investigations of crystalline compounds [42,66–68] or model substances with isolated two-spin systems [69,70], while applications to dipolar coupled many-spin systems have not yet been reported. Aside from a recently reported Monte Carlo (MC) based modeling of RESPDOR curves for amorphous silica materials [71], there is no report on measurements or modeling of RESPDOR experiments on glasses, to the best of our knowledge. The work by Perras et al., introduced for ${}^{29}\text{Si}$ observed experiments, simulates several W-RESPDOR curves given all the permutations of possible second-coordination spheres of the four-coordinated Si, in which Al and Si atoms occur in the second coordination sphere [71]. While this model describes well the RESPDOR curves measured in the binary amorphous SiO₂-Al₂O₃ system, it is more limited for structural scenarios in which several coordination environments of the observed nuclear species may occur. Especially in the case of network-modifier-observed experiments in glasses, the distribution of coordination numbers is often unknown. Therefore, in the present contribution, we have taken a different approach to demonstrate that

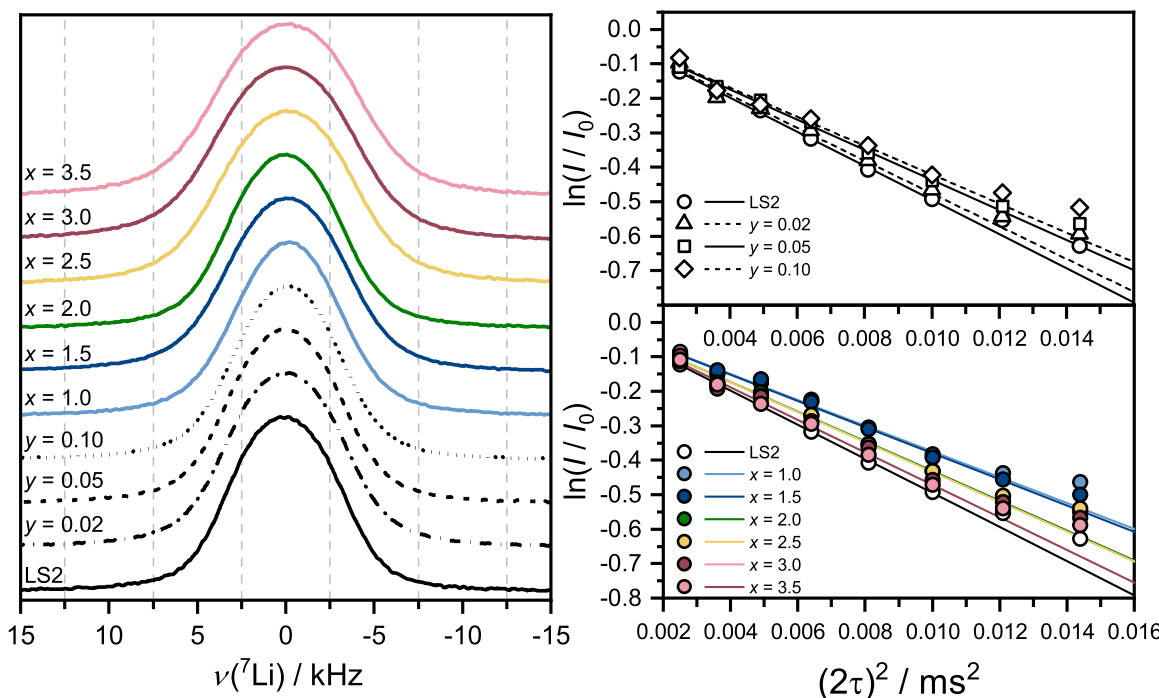


Fig. 7. Static ${}^7\text{Li}$ NMR spectra (left) and ${}^7\text{Li}$ spin echo decay curves (right) of the glasses under study. The experimental errors correspond to the symbol sizes.

the initial dephasing behavior of a W-RESPDOR curve can be modeled by a parabolic approximation, yielding a dipolar second-moment corresponding to the average dipolar coupling strength of the spin system along the lines of previous REDOR data treatments and analyses [43]. This approach is justified by SIMPSON simulations (see Fig. S1 in the supporting information), which show that the W-RESPDOR dephasing curves of a spin 3/2 – spin 9/2 pair are only rather weakly influenced by the geometry of the spin system and by the exact symmetry and relative orientation of dipolar and EFG tensors and the external magnetic field. The initial dipolar-mixing time regime, similar to the situation in the REDOR experiment, thus reflects the average dipolar interaction strength of the spin system which can be modeled by the analytical expression (see Eq (4)). In Section S2 of the Supporting Information Section, we derive a parabolic approximation of the W-RESPDOR dephasing curve based on the analytically modeled dephasing curve for a two-spin system, where the recoupled spin has spin quantum number S . This way, the evaluation of (W)-RESPDOR curves can be further facilitated. Additionally, rather than introducing a correction factor f to account for saturation inefficiencies, in the following, we investigated the effect of non-ideal saturation due to the presence of a Czjzek distribution of quadrupolar interaction parameters for a WURST pulse with 400 μ s duration, 450 kHz sweep-width and shape parameter $N = 80$.

We found the latter to be effective for quadrupolar coupling constants up to about 80 MHz. To this end, we used SIMPSON to calculate a simulation map covering a wide parameter space of C_Q and η_Q and analyzed the residual z-component magnetization I_z for Czjzek distributions with varying distribution widths σ , see Fig. 8. Given the herein-employed WURST saturation pulse, the residual z-magnetization is nearly zero for $\sigma = 11$ MHz ($|C_Q| \approx 22$ MHz) and decreases linearly to about 0.15 for $\sigma = 35$ MHz. Given that the experimentally found σ values lie in the order of about 24 MHz (see Table 4), we conclude that the experimental ${}^7\text{Li}\{{}^{93}\text{Nb}\}$ second moments are likely somewhat underestimated.

Further, the inset of Fig. 8 shows how incomplete saturation of the ${}^{93}\text{Nb}$ spin system affects the W-RESPDOR curves. We have simulated W-RESPDOR curves for two-spin systems assuming a fixed ${}^7\text{Li}\{{}^{93}\text{Nb}\}$ effective two-spin distance of 2.24 Å, corresponding to the $M_{2(\text{Li-Nb})}$ of the multi-spin interaction in LiNbO_3 (271×10^6 rad $^2/\text{s}^2$), and ${}^{93}\text{Nb}$ quadrupolar parameters according to the same Czjzek distribution as determined above. The resulting curves, after weighted averaging according

to Czjzek distributions at a given σ , are shown in the inset of Fig. 8 together with the dephasing curve of a two-spin system assuming the C_Q value of LiNbO_3 (21.9 MHz). We find that the underestimation of the first data point ($NT_r = 0.1$ ms and $\Delta S/S_0 \approx 0.3$), while minor, is proportional to the magnitude of the residual magnetization. For the simulations with $\sigma = 30$ MHz, where there is weaker dephasing, the dipolar coupling constant obtained through Eq. (4) is, correspondingly, lower by 13%, comparable to the residual magnetization of 0.13, possibly by coincidence. Thus, we conclude that in the present case, no correction factor is required for recoupling experiments involving ${}^{93}\text{Nb}$, considering an estimated general uncertainty of about $\pm 10\%$, often also estimated from REDOR experiments.

Fig. 9 shows ${}^7\text{Li}\{{}^{93}\text{Nb}\}$ -W-RESPDOR curves for LiNbO_3 and the glasses under study. For LiNbO_3 , the data are compared to a simulated curve for a two-spin system, using an effective value of the dipolar coupling constant (1020 Hz) calculated from the crystallographic second moment. They are also compared to the analytical expression given in Eq. (4). For the glasses, the experimental data are fitted to a parabola, i.e., the first term of Eq. (5), in the initial dipolar mixing regime of $\Delta S/S_0 < 0.2$, while fits to the latter are shown in Fig. S2. The extracted moments are shown in Tables 6 and S2, respectively.

Note that for the model compound, the experimental data are in good agreement with the simulated curves based on the crystallographic information (despite being treated as a two-spin interaction) further validating our approach. However, deviations between the experimental and the simulated data can be seen for dipolar mixing times beyond 0.4 ms. The results obtained on the (1-y) $\text{LS}_2\text{-yNb}_2\text{O}_5$ glasses show the expected compositional trend, indicating that with increasing Nb_2O_5 content ($\text{Nb}_2\text{O}_5/\text{Li}_2\text{O}$ ratio) the ${}^7\text{Li}\{{}^{93}\text{Nb}\}$ dipole-dipole coupling strength increases. For the SiO_2 -[(Li_2O)_{1.4}-(Nb_2O_5)] glasses, the second moments are nearly independent of composition, which is consistent with their constant Nb/Li ratio of 0.71. This result, again, suggests that the local environment of Nb and the distribution of Li relative to Nb is principally influenced by the total $\text{Li}_2\text{O}/\text{Nb}_2\text{O}_5$ ratio.

3.7. Molecular dynamics simulations

Table 7 summarizes the main results from the molecular dynamics simulations. For LS2 glass, the potential by Sun et al. used here gives a very similar result as the potential by Pedone et al. [72] used in a recent study by some of the authors. In this table, the superscript n used for the

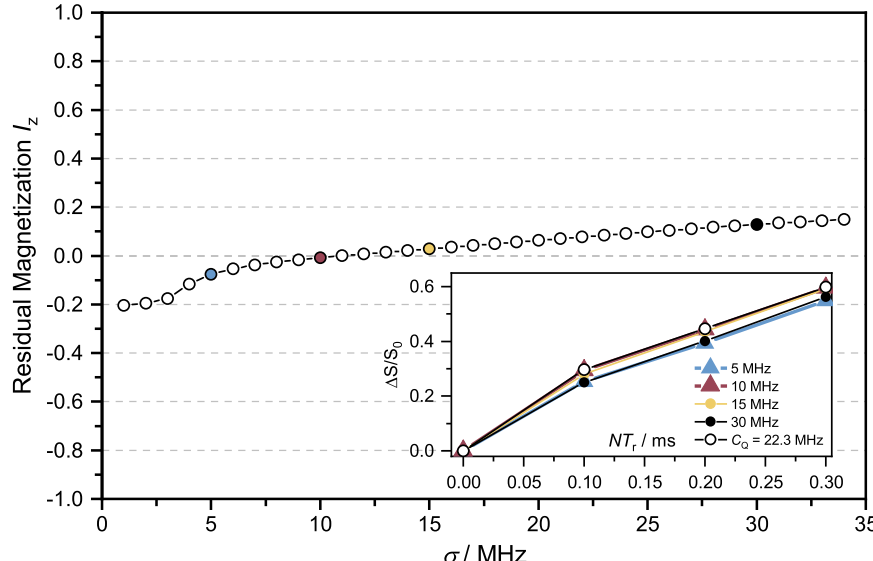


Fig. 8. Residual magnetization I_z after saturation of a ${}^{93}\text{Nb}$ spin system with a given Czjzek distribution width σ . The inset shows the first points of simulated W-RESPDOR curves considering the indicated Czjzek distribution widths and a ${}^7\text{Li}\{{}^{93}\text{Nb}\}$ two-spin system with an effective distance of 2.4 Å corresponding to the $M_{2(\text{Li-Nb})}$ of LiNbO_3 .

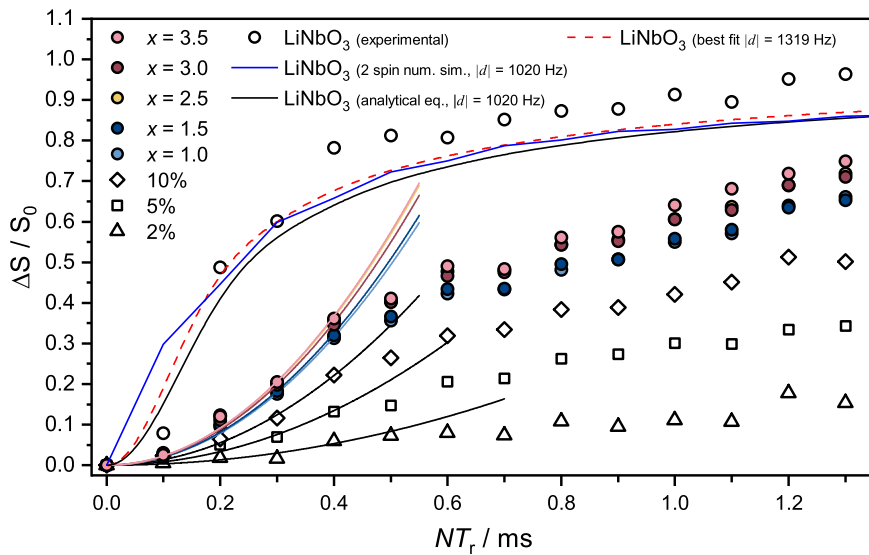


Fig. 9. Experimental and calculated $^7\text{Li}\{{}^{93}\text{Nb}\}\text{W}$ -RESPDOR dephasing curves for crystalline LiNbO_3 and the samples under study. For LiNbO_3 , blue and black solid curves are simulated curves based on the theoretically expected $M_{2(\text{Li}-\text{Nb})}$ value from the crystal structure, expressed in terms of an effective internuclear Li-Nb distance, using the numerical simulation and the analytical approximation (Eq. (4)), respectively. The dashed curve denotes a simulation using the analytical approximation with an adjusted effective distance, giving better agreement with the experimental data. For the glasses, solid curves are fits to the data constrained to the initial dephasing regime $\Delta S/S_0 \leq 0.2$, using the parabolic approximation (Eq. (5)) of the theoretical saturation-based recoupling curve for $I = 9/2$, see Eq. (4) [42,70].

different Nb^n species again denotes the number of bridging oxygen atoms.

However, the results are unsatisfactory for all the Nb-containing glasses, as they most likely underestimate the amount of $\text{Nb}-\text{O}-\text{Nb}$ connectivity suggested by the Raman spectra. Also, the Si^n speciation shows very poor agreement with the experimental ^{29}Si MAS-NMR data, even though they qualitatively reproduce the dependence on composition. Finally, Fig. 10 indicates that the MD simulations produce large discrepancies between the theoretically predicted values of $M_{2(\text{Li}-\text{Nb})}$ and $M_{2E(\text{Li}-\text{Li})}$ and the experimental data.

The discrepancies are particularly large concerning the $M_{2E(\text{Li}-\text{Li})}$ prediction in the LS2-based system and the $M_{2(\text{Li}-\text{Nb})}$ prediction in the LNS system. We thus conclude that the MD simulations do not correctly capture the structural organization of these glasses. They tend to overestimate the attraction of the network modifier by the niobium species

and hence lead to silicate networks that are much more polymerized (having lower numbers of NBO-bearing silicate species) than found experimentally. Possibly, as these empirical potentials were developed based on LiNbO_3 , some bias may exist for the preferential charge compensation of $[\text{NbO}_6]^-$ units by Li^+ ions. It should be noted that in their study [46], the authors investigated SiO_2 - $[\text{Li}_2\text{O}-\text{Nb}_2\text{O}_5]$ glasses with a $\text{Li}_2\text{O}/\text{Nb}_2\text{O}_5$ ratio of unity. It would be interesting to measure ^{29}Si MAS NMR data on this glass system, which could provide an independent test of the ability of their MD simulations to predict the correct Si^n speciation.

4. Discussion

Based on the above experimental and simulation results, the compositional evolution of the $(1-y)\text{LS2}-y\text{Nb}_2\text{O}_5$ system can be

Table 7
Species distribution of Si and Nb from MD simulations.

MD	(1-y)LS2-yNb ₂ O ₅				Composition x					
	Si ⁿ / % (± 0.5)	0	0.02	0.05	0.10	1.0	1.5	2.0	2.5	3.0
Si ⁰	0.2	0.3	0	0	-	-	-	-	-	-
Si ¹	3.7	3.2	2.3	0.8	0.1	0.1	-	-	-	0.2
Si ²	21.4	18.4	13.8	8.4	1.9	3.2	-	-	-	5.1
Si ³	44.7	42.7	41.9	35.3	22.6	28.2	-	-	-	29.7
Si ⁴	30.0	35.4	42.0	55.5	75.4	68.5	-	-	-	65.0
Nb Q ⁿ / % (± 0.5)	0	0.02	0.05	0.1	1.0	1.5	2.0	2.5	3.0	3.5
Nb ⁰	-	-	-	-	-	-	-	-	-	-
Nb ¹	-	-	-	-	-	-	-	-	-	-
Nb ²	-	-	-	0.4	-	-	-	-	-	-
Nb ³	-	0.7	0.3	0.2	-	-	-	-	-	0.2
Nb ⁴	-	8.4	6.5	6.6	2.2	2.2	-	-	-	4.3
Nb ⁵	-	29.2	33.7	26.0	18.3	22.9	-	-	-	30.3
Nb ⁶	-	61.7	59.5	66.8	79.5	74.9	-	-	-	65.2

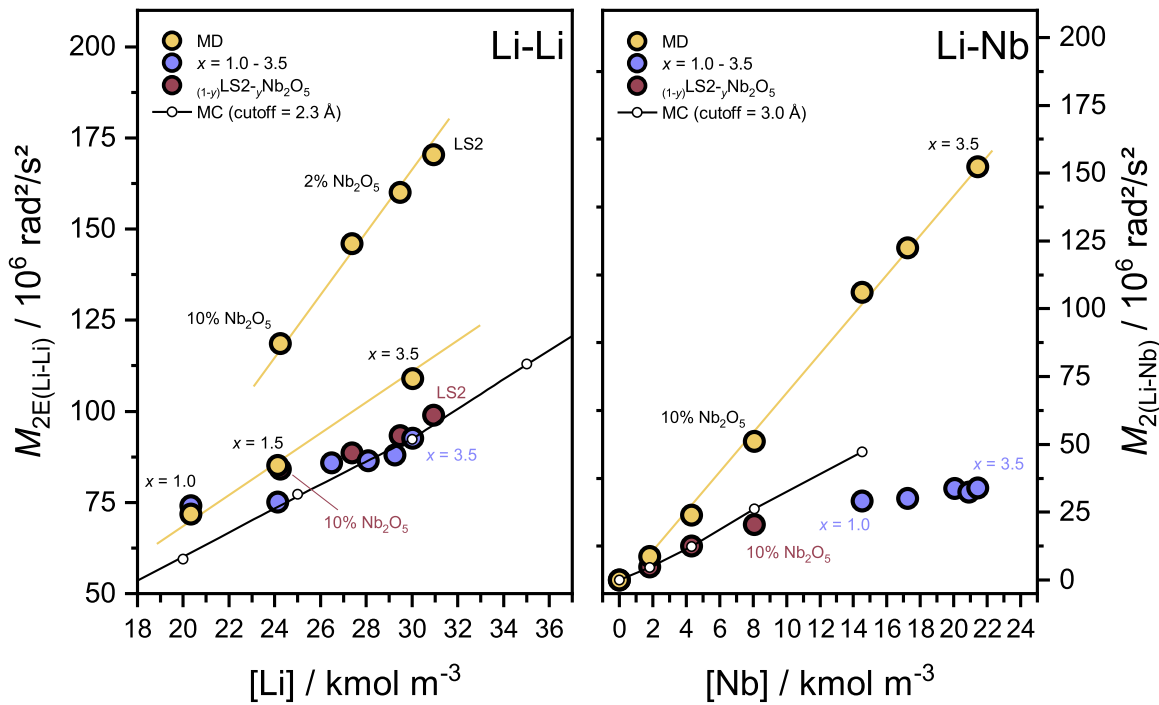


Fig. 10. Homonuclear $M_{2E(Li-Li)}$ (left) and heteronuclear $M_{2(Li-Nb)}$ (right) values measured on the glasses under study and from MD and MC simulations.

described as follows: Pentavalent niobium enters the structure in the form of a six-coordinated anionic species, creating Si-O-Nb linkages, thereby converting Si^3 to Si^4 units in a process similar to the effect of alumina in alkali silicate glasses. Thus, the process enhances the extent of network connectivity, accounting for an increase in the glass transition temperature with increasing Nb_2O_5 content. From the non-bridging oxygen balance, one must conclude, however, that the fraction of the lithium inventory invested in the accommodation of such anionic niobium species in the network in this manner is lower than unity, amounting to ca. 0.7 per Nb atom. Nevertheless, the partial transformation of the niobium species into an anionic site suggests that the transition metal oxide should be considered a network former species. At low y -values, the NbO_6 units appear to have more connectivity to silica than at higher y -values, according to the common interpretation of our Raman data. Thus, with an increasing degree of substitution, more Nb-O-Nb linkages and other types of connectivity, such as edge-sharing, may appear. The repolymerization of the silica species also results in a re-distribution of the lithium inventory, resulting in weaker ${}^7\text{Li}$ - ${}^7\text{Li}$ dipole-dipole interactions than in lithium disilicate glass.

For the LNS glass system, which corresponds to the SiO_2 - $[(\text{Li}_2\text{O})_{1.4}(\text{Nb}_2\text{O}_5)]$ substitution series, the majority of the lithium inventory is used to create non-bridging oxygen on the silica network. This results in a substantial degree of depolymerization, from $\langle n_{\text{Si}} \rangle = 3.31$ in a glass with approximate composition 50SiO_2 - $29\text{Li}_2\text{O}$ - $21\text{Nb}_2\text{O}_5$ ($x = 1.0$) to $\langle n_{\text{Si}} \rangle = 2.10$ in a glass with approximate composition 22SiO_2 - $45\text{Li}_2\text{O}$ - $33\text{Nb}_2\text{O}_5$ ($x = 3.5$). The connectivity analysis leads to the conclusion that also for this system on average each formula unit of Nb_2O_5 requires about 0.66 ± 0.15 equivalents of Li_2O for its accommodation as a network former species. As expected, the strength of the ${}^7\text{Li}$ - ${}^7\text{Li}$ dipole-dipole interactions as characterized by $M_{2E(Li-Li)}$ increases with increasing Li_2O content in this compositional series, whereas the strength of the ${}^7\text{Li}$ - ${}^{93}\text{Nb}$ dipole-dipole interactions as characterized by $M_{2(Li-Nb)}$ remains more or less constant. The latter is not unexpected because the Li/Nb ratio remains fixed within this compositional series. All of these results are consistent with an essentially random distribution of lithium ions, both with respect to each other and to the niobium species. Fig. 10 nicely confirms this result through a Monte Carlo simulation which closely matches the experimental data for $M_{2(Li-Li)}$

over the whole range of Li contents investigated and for $M_{2(Li-Nb)}$ over the range of Nb concentrations for which a random distribution box for Li-Nb distance evaluation could be generated. In this MC simulation, the cut-off values for Li-Li distances were put at 2.30 \AA , whereas for the Li-Nb cut-off distance, a value of 3.3 \AA was chosen. To examine how sensitive the experimental results are to the choice of correct cutoff distance, the corresponding MC predictions for different cutoff distances are listed in the supporting Materials Section, see Fig. S4. Considering the composition $y = 0.10$, within sensible limits of cutoff values of $2.2 - 2.4 \text{ \AA}$ for Li-Li distances and of $2.9 - 3.3 \text{ \AA}$ for Li-Nb distances, the variation in the simulated $M_{2(Li-Nb)}$ and $M_{2E(Li-Li)}$ data is about $\pm 4 \times 10^6 \text{ rad}^2/\text{s}^2$ (ranging from 36 to $28 \times 10^6 \text{ rad}^2/\text{s}^2$), and $\pm 11 \times 10^6 \text{ rad}^2/\text{s}^2$ (ranging from 88 to $66 \times 10^6 \text{ rad}^2/\text{s}^2$) respectively. Based on this $\sim 15\%$ variation in the simulated $M_{2(Li-Nb)}$ values, the conclusion about the random distribution of Li is sufficiently robust. On the other hand, at higher Nb concentrations, the experimental data deviate from the linear dependence on Nb concentration, which may be indicative of some Nb clustering. This finding is compatible with the Raman spectroscopic data, which are independent of composition for $x > 1$ and also indicate a propensity of Nb to form Nb-O-Nb linkages at these higher concentrations.

Lastly, we point out that the herein obtained results do not agree with the conclusions proposed in a recent ${}^{93}\text{Nb}$ MAS NMR study on Nb-containing aluminosilicate glasses [73] where the authors claimed to have observed a wide distribution of Nb_n species, with $n = \{4, 5, 6, 7, 8\}$ based on an incorrect analysis (Gaussian deconvolution) of MAS-NMR spectra obtained with insufficient spinning rates (20 kHz). The present contribution based on a Czjzek analysis of spectra obtained with much faster spinning rates (60 kHz) gives no evidence for Nb species with coordination numbers different from six in niobium oxide-containing lithium disilicate glasses.

An issue requiring more detailed work in the future concerns the analysis and interpretation of the ${}^{93}\text{Nb}$ NMR results also obtained in the present study. Owing to the intrinsic nature of the glassy state, the NMR parameters are not uniquely defined by singular values as they are in crystals but are subject to distribution functions that greatly impact the NMR spectra. While the Czjzek model certainly provides a convenient way of modeling spectra affected by distributions of second-order

quadrupolar effects, we find that the analysis of ^{93}Nb NMR spectra in glasses encounters certain limitations arising from the effect of non-negligible chemical shift anisotropy, requiring field-dependent spectral analyses and simulations for separating these interactions. Furthermore, DFT calculations are required to clarify the relation of chemical shift anisotropies, electric field gradients, and their distributions with the different possible niobium coordination environments in oxide glasses. Further experimental work will involve spectral editing via ^{93}Nb detected dipolar spectroscopy at high spinning speeds ($> 60 \text{ kHz}$) and ^{17}O NMR work on isotopically enriched glasses for differentiation between corner- and edge-sharing modes. The results of these efforts will be reported at a later stage.

5. Conclusions

The present study details new important information about the role of niobium oxide on the medium-range order of alkali silicate glasses; in this case, Li silicate. To the best of our knowledge, we report RESPDOR experiments and modeling on glasses for the first time. All the data are consistent with a *network former* role of Nb_2O_5 , whose accommodation in the glasses in the form of corner- and edge-shared octahedra requires, on average, 0.7 equivalents of Li_2O , leading to profound changes in the degree of polymerization of the silica component, the local environments of the lithium ions and their spatial distribution. The average homo- and heteronuclear dipolar interaction strengths, as expressed by the second moments $M_{2(\text{Li-Li})}$ and $M_{2(\text{Li-Nb})}$, are consistent with random spatial distributions of the lithium ions with respect to themselves and the niobium species and with the Monte Carlo simulations presented herein. This conclusion holds particularly for the LS2 system, whereas in the LNS system, a tendency of Nb clustering can be noted at higher x -values. Altogether the current study defines a comprehensive investigative strategy for elucidating the structural impact of (NMR active) intermediate oxides incorporated into silicate glasses.

Declaration of Competing Interest

The authors declare that they have no known competing financial interests or personal relationships that could have appeared to influence the work reported in this paper.

Acknowledgments

This work was supported by the São Paulo Research Foundation (FAPESP) under grant no. 2013/07793–6 (CEPID program). H.B. and A. G. are grateful for the post-doctoral support received from FAPESP under grant numbers 2019/26399–3 and 2021/06370–0, respectively. HE (310870/2020–8) and EDZ (303886/2015–3) are grateful to CNPq for a Bolsa de Pesquisa Grant. We kindly thank Dr. Silvia H. Santagneli (Chemistry Department, UNESP, Araraquara, Brazil) for measuring the Raman spectra and Dr. Maria Rita Cicconi (Materials Science Department, FAU, Erlangen, Germany), for valuable discussions. Finally, QZ and EDZ are grateful to CBMM (Cia. Brasileira de Mineração e Metalurgia) for research grants dedicated to revealing the role of Nb_2O_5 in the physical-chemical properties of silicate glasses.

Supplementary materials

Supplementary material associated with this article can be found, in the online version, at [doi:10.1016/j.actamat.2023.119061](https://doi.org/10.1016/j.actamat.2023.119061).

References

- [1] M.E. Lines, Influence of d orbitals on the nonlinear optical response of transparent transition-metal oxides, *Phys. Rev. B* 43 (14) (1991) 11978–11990.
- [2] B.G. Aitken, High Refractive Index Titanium-Niobium Phosphate Glass, W.I.P. Organization (Ed.) 2018.
- [3] D. Manzani, T. Gualberto, J.M.P. Almeida, M. Montesso, C.R. Mendonça, V.A. G. Rivera, L. De Boni, M. Nalin, S.J.L. Ribeiro, Highly nonlinear $\text{Pb}_2\text{P}_2\text{O}_7\text{-Nb}_2\text{O}_5$ glasses for optical fiber production, *J. Non Cryst. Solids* 443 (2016) 82–90.
- [4] L.M. Marcondes, L. Rodrigues, C. Ramos da Cunha, R.R. Gonçalves, A.S.S. de Camargo, F.C. Cassanjes, G.Y. Poirier, Rare-earth ion doped niobium germanate glasses and glass-ceramics for optical device applications, *J. Lumin.* 213 (2019) 224–234.
- [5] L.M. Marcondes, R.O. Evangelista, R.R. Gonçalves, A.S.S. de Camargo, D. Manzani, M. Nalin, F.C. Cassanjes, G.Y. Poirier, Er^{3+} -doped niobium alkali germanate glasses and glass-ceramics: NIR and visible luminescence properties, *J. Non Cryst. Solids* 521 (2019), 119492.
- [6] J.H. Faleiro, N.O. Dantas, A.C.A. Silva, H.P. Barbosa, B.H.S.T. da Silva, K.d. O. Lima, G.d.F. Silva, R.R. Gonçalves, R. Falci, Y. Messadeq, I.D.d.O. Branco, B. M. Cerruti, H. Bradtmüller, H. Eckert, J.L. Ferrari, Niobium incorporation into rare-earth doped aluminophosphate glasses: structural characterization, optical properties, and luminescence, *J. Non Cryst. Solids* 605 (2023), 122173.
- [7] P.A. Loiko, O.S. Dymshits, I.P. Alekseeva, A.A. Zhilin, M.Y. Tsenter, E. V. Vilejshikova, K.V. Bogdanov, X. Mateos, K.V. Yumashev, Transparent glass-ceramics with $(\text{Eu}^{3+},\text{Yb}^{3+})_x\text{NbO}_4$ nanocrystals: crystallization, structure, optical spectroscopy and cooperative upconversion, *J. Lumin.* 179 (2016) 64–73.
- [8] X. Lia, J. Li, J. Li, H. Lin, B. Li, Upconversion $32\text{Nb}_2\text{O}_5\text{-}10\text{La}_2\text{O}_3\text{-}16\text{ZrO}_2$ glass activated with $\text{Er}^{3+}/\text{Yb}^{3+}$ and dye sensitized solar cell application, *J. Adv. Ceram.* 6 (4) (2017) 312–319.
- [9] M.P. Fernandes Graça, M.A. Valente, Ferroelectric glass-ceramics, *MRS Bull.* 42 (2017) 213–219.
- [10] T. Srihari, C.K. Jayasankar, Fluorescence properties and white light generation from Dy^{3+} -doped niobium phosphate glasses, *Opt. Mater.* 69 (2017) 87–95.
- [11] S. Dai, J. Wu, J. Zhang, G. Wang, Z. Jiang, The spectroscopic properties of Er^{3+} -doped $\text{TeO}_2\text{-Nb}_2\text{O}_5$ glasses with high mechanical strength performance, *Spectrochim. Acta A Mol. Biomol. Spectrosc.* 62 (1) (2005) 431–437.
- [12] M. Dussauze, E.I. Kamitsos, E. Fargin, V. Rodriguez, Structural rearrangements and second-order optical response in the space charge layer of thermally poled sodium–niobium borophosphate glasses, *J. Phys. Chem. C* 111 (39) (2007) 14560–14566.
- [13] Y. Jia, L. Wang, F. Chen, Ion-cut lithium niobate on insulator technology: recent advances and perspectives, *Appl. Phys. Rev.* 8 (1) (2021), 011307.
- [14] A. Honardoost, K. Abdelsalam, S. Pathpour, Rejuvenating a versatile photonic material: thin-film lithium niobate, *Laser Photonics Rev.* 14 (9) (2020), 2000088.
- [15] A. Aronne, V.N. Sigaev, B. Champagnon, E. Fanelli, V. Califano, L.Z. Usmanova, P. Pernice, The origin of nanostructuring in potassium niobiosilicate glasses by Raman and FTIR spectroscopy, *J. Non Cryst. Solids* 351 (46) (2005) 3610–3618.
- [16] K. Fukumi, S. Sakka, Coordination state of Nb^{5+} ions in silicate and gallate glasses as studied by Raman spectroscopy, *J. Mater. Sci.* 23 (8) (1988) 2819–2823.
- [17] G. Huanxin, W. Zhongcai, W. Shizhuo, Properties and structure of niobiosilicate glasses, *J. Non Cryst. Solids* 112 (1) (1989) 332–335.
- [18] A.A. Lipovskii, D.K. Tagantsev, A.A. Vetrov, O.V. Yanush, Raman spectroscopy and the origin of electrooptical Kerr phenomenon in niobium alkali-silicate glasses, *Opt. Mater.* 21 (4) (2003) 749–757.
- [19] T. Fuss, A. Moguš-Milanković, C.S. Ray, C.E. Lesher, R. Youngman, D.E. Day, Ex situ XRD, TEM, IR, Raman and NMR spectroscopy of crystallization of lithium disilicate glass at high pressure, *J. Non Cryst. Solids* 352 (38) (2006) 4101–4111.
- [20] L.M. Marcondes, S. Maestri, B. Sousa, R.R. Gonçalves, F.C. Cassanjes, G.Y. Poirier, High niobium oxide content in germanate glasses: thermal, structural, and optical properties, *J. Am. Ceram. Soc.* 101 (1) (2018) 220–230.
- [21] M.R. Cicconi, D.K. Dobesh, B. Schroeder, T. Otsuka, T. Hayakawa, D. de Ligny, Alkali-Niobate aluminosilicate glasses: structure and properties, *Opt. Mater. X* 18 (2023), 100228.
- [22] A. Flambard, J.J. Videau, L. Delevoye, T. Cardinal, C. Labrugère, C.A. Rivero, M. Couzi, L. Montagne, Structure and nonlinear optical properties of sodium–niobium phosphate glasses, *J. Non Cryst. Solids* 354 (30) (2008) 3540–3547.
- [23] S. Chenu, U. Werner-Zwanziger, C. Calahoo, J.W. Zwanziger, Structure and properties of $\text{NaPO}_3\text{-ZnO-Nb}_2\text{O}_5\text{-Al}_2\text{O}_3$ glasses, *J. Non Cryst. Solids* 358 (15) (2012) 1795–1805.
- [24] M. Dolhen, M. Allix, V. Sarou-Kanian, F. Fayon, C. Genevois, S. Chenu, P.-E. Coulon, M. Colas, J. Cornette, J.-R. Duclère, F. Brisset, O. Masson, P. Thomas, G. Delaizir, A comprehensive study of the glass/translucent anti-glass/transparent ceramic structural ordering in the $\text{Bi}_2\text{O}_3\text{-Nb}_2\text{O}_5\text{-TeO}_2$ system, *Acta Mater.* 189 (2020) 73–84.
- [25] L.M. Marcondes, H. Bradtmüller, S.N. Carvalho dos Santos, L.K. Nolasco, C. R. Mendonça, S.H. Santagneli, G.Y. Poirier, M. Nalin, Structural and luminescence characterization of europium-doped niobium germanate glasses and glass-ceramics: novel insights from ^{93}Nb solid-state NMR spectroscopy, *Ceram. Int.* 48 (14) (2022) 20801–20808.
- [26] K.O. Drake, D. Carta, L.J. Skipper, F.E. Sowrey, R.J. Newport, M.E. Smith, A multinuclear solid state NMR study of the sol-gel formation of amorphous $\text{Nb}_2\text{O}_5\text{-SiO}_2$ materials, *Solid State Nucl. Magn. Reson.* 27 (1) (2005) 28–36.
- [27] R.T. Hart, M.A. Anspach, B.J. Kraft, J.M. Zaleski, J.W. Zwanziger, P.J. DeSanto, B. Stein, J. Jacob, P. Thiagarajan, Optical Implications of crystallite symmetry and structure in potassium niobate tellurite glass ceramics, *Chem. Mater.* 14 (10) (2002) 4422–4429.
- [28] A. Flambard, L. Montagne, L. Delevoye, G. Palavit, J.-P. Amoureux, J.-J. Videau, Solid-state NMR study of mixed network sodium–niobium phosphate glasses, *J. Non Cryst. Solids* 345 (346) (2004) 75–79.
- [29] P. Prapitpongwanich, K. Pengpat, C. Rüssel, Phase separation and crystallization in $\text{LiNbO}_3\text{/SiO}_2$ glasses, *Mater. Chem. Phys.* 113 (2) (2009) 913–918.

- [30] C. Jäger, W. Müller-Warmuth, C. Mundus, L. van Wüllen, ^{27}Al MAS-NMR spectroscopy of glasses: new facilities by application of 'SATRAS', *J. Non Cryst. Solids* 149 (3) (1992) 209–217.
- [31] G. Czjzek, J. Fink, F. Götz, H. Schmidt, J.M.D. Coey, J.P. Rebouillat, A. Liénard, Atomic coordination and the distribution of electric field gradients in amorphous solids, *Phys. Rev. B* 23 (6) (1981) 2513–2530.
- [32] S.G.J. van Meerten, W.M.J. Franssen, A.P.M. Kentgens, ssNake: a cross-platform open-source NMR data processing and fitting application, *J. Magn. Reson.* 301 (2019) 56–66.
- [33] M. Bak, J.T. Rasmussen, N.C. Nielsen, SIMPSON: a general simulation program for solid-state NMR spectroscopy, *J. Magn. Reson.* 147 (2) (2000) 296–330.
- [34] J.G. Longstaffe, U. Werner-Zwanziger, J.F. Schneider, M.L. Nascimento, E. D. Zanotto, J.W. Zwanziger, Intermediate-range order of alkali disilicate glasses and its relation to the devitrification mechanism, *J. Phys. Chem. C* 112 (15) (2008) 6151–6159.
- [35] D. Lathrop, D. Franke, R. Maxwell, T. Tepe, R. Flesher, Z. Zhang, H. Eckert, Dipolar ^{31}P NMR spectroscopy of crystalline inorganic phosphorus compounds, *Solid State Nucl. Magn. Reson.* 1 (2) (1992) 73–83.
- [36] B. Gee, H. Eckert, ^{23}Na nuclear magnetic resonance spin echo decay spectroscopy of sodium silicate glasses and crystalline model compounds, *Solid State Nucl. Magn. Reson.* 5 (1) (1995) 113–122.
- [37] J.H. Van Vleck, The dipolar broadening of magnetic resonance lines in crystals, *Phys. Rev.* 74 (9) (1948) 1168.
- [38] J. Haase, E. Oldfield, Spin-echo behavior of nonintegral-spin quadrupolar nuclei in inorganic solids, *J. Magn. Reson. A* 101 (1) (1993) 30–40.
- [39] M. Makrinič, E. Nimerovsky, A. Goldbourt, Pushing the limit of NMR-based distance measurements – retrieving dipolar couplings to spins with extensively large quadrupolar frequencies, *Solid State Nucl. Magn. Reson.* 92 (2018) 19–24.
- [40] E. Kupce, R. Freeman, Adiabatic pulses for wideband inversion and broadband decoupling, *J. Magn. Reson. A* 115 (2) (1995) 273–276.
- [41] A.-L. Wübker, J. Koppe, H. Bradtmüller, L. Keweloh, D. Pleschka, W. Uhl, M. R. Hansen, H. Eckert, Solid-state nuclear magnetic resonance techniques for the structural characterization of geminal alane-phosphane frustrated lewis pairs and secondary adducts, *Chem. Eur. J.* 27 (52) (2021) 13249–13257.
- [42] E. Nimerovsky, R. Gupta, J. Yehl, M. Li, T. Polenova, A. Goldbourt, Phase-modulated LA-REDOR: a robust, accurate and efficient solid-state NMR technique for distance measurements between a spin-1/2 and a quadrupole spin, *J. Magn. Reson.* 244 (2014) 107–113.
- [43] M. Bertmer, H. Eckert, Dephasing of spin echoes by multiple heteronuclear dipolar interactions in rotational echo double resonance NMR experiments, *Solid State Nucl. Magn. Reson.* 15 (3) (1999) 139–152.
- [44] A.P. Thompson, H.M. Aktulga, R. Berger, D.S. Bolintineanu, W.M. Brown, P. S. Crozier, P.J. in't Veld, A. Kohlmeyer, S.G. Moore, T.D. Nguyen, LAMMPS-a flexible simulation tool for particle-based materials modeling at the atomic, meso, and continuum scales, *Comput. Phys. Commun.* 271 (2022), 108171.
- [45] S. Plimpton, Fast parallel algorithms for short-range molecular dynamics, *J. Comput. Phys.* 117 (1) (1995) 1–19.
- [46] W. Sun, K. Veenhuizen, J. Marsh, V. Dierolf, H. Jain, Determination of the structure of lithium niobosilicate glasses by molecular dynamics simulation with a new Nb-O potential, *Comput. Mater. Sci.* 207 (2022), 111307.
- [47] L. Verlet, Computer "experiments" on classical fluids. i. thermodynamical properties of lennard-jones molecules, *Phys. Rev.* 159 (1) (1967) 98–103.
- [48] S. Nosé, A unified formulation of the constant temperature molecular dynamics methods, *J. Chem. Phys.* 81 (1) (1984) 511–519.
- [49] W. Shinoda, M. Shiga, M. Mikami, Rapid estimation of elastic constants by molecular dynamics simulation under constant stress, *Phys. Rev. B* 69 (13) (2004), 134103.
- [50] O.N. Koroleva, T.N. Ivanova, Raman spectroscopy of the structures of $\text{Li}_2\text{O}-\text{SiO}_2$ and $\text{Li}_2\text{O}-\text{GeO}_2$ melts, *Russ. Metall. (Met.)* 2014 (2) (2014) 140–146.
- [51] K. Fukumi, T. Kokubo, K. Kamiya, S. Sakka, Structures of alkali niobium gallate glasses, *J. Non Cryst. Solids* 84 (1–3) (1986) 100–104.
- [52] B. Yu, B. Chen, X. Yang, J. Qiu, X. Jiang, C. Zhu, K. Hirao, Study of crystal formation in borate, niobate, and titanate glasses irradiated by femtosecond laser pulses, *J. Opt. Soc. Am. B* 21 (1) (2004) 83–87.
- [53] T. Komatsu, K. Koshiba, T. Honma, Preferential growth orientation of laser-patterned LiNbO_3 crystals in lithium niobium silicate glass, *J. Solid State Chem.* 184 (2) (2011) 411–418.
- [54] N.M. Ferreira, M.C. Ferro, M.P.F. Graça, F.M. Costa, Effect of laser irradiation on lithium niobate powders, *Ceram. Int.* 43 (2) (2017) 2504–2510.
- [55] T.M. Anderson, S.G. Thoma, F. Bonhomme, M.A. Rodriguez, H. Park, J.B. Parise, T. M. Alam, J.P. Larentzos, M. Nyman, L. Polyniobates, A Lindqvist-supported lithium–water adamantane cluster and conversion of hexaniobate to a discrete Keggin complex, *Cryst. Growth Des.* 7 (4) (2007) 719–723.
- [56] H. Bradtmüller, A. Gaddam, H. Eckert, E.D. Zanotto, Structural rearrangements during sub- T_g relaxation and nucleation in lithium disilicate glass revealed by a solid-state NMR and MD strategy, *Acta Mater.* (2022), 118318.
- [57] O.B. Lapina, D.F. Khabibulin, K.V. Romanenko, Z. Gan, M.G. Zuev, V. N. Krasil'nikov, V.E. Fedorov, ^{93}Nb NMR chemical shift scale for niobia systems, *Solid State Nucl. Magn. Reson.* 28 (2) (2005) 204–224.
- [58] S. Prasad, P. Zhao, J. Huang, J.J. Fitzgerald, J.S. Shore, Niobium-93 MQMAS NMR spectroscopic study of alkali and lead niobates, *Solid State Nucl. Magn. Reson.* 19 (1) (2001) 45–62.
- [59] J. Davis, D. Tinet, J.J. Fripiat, J.M. Amarilla, B. Casal, E. Ruiz-Hitzky, ^{51}V and ^{93}Nb high resolution NMR study of NbVO_5 , *J. Mater. Res.* 6 (2) (1991) 393–400.
- [60] C. Nico, T. Monteiro, M.P.F. Graça, Niobium oxides and niobates physical properties: review and prospects, *Prog. Mater. Sci.* 80 (2016) 1–37.
- [61] B.M. Gatehouse, A.D. Wadsley, The crystal structure of the high temperature form of niobium pentoxide, *Acta Crystallogr.* 17 (12) (1964) 1545–1554.
- [62] D. Khabibulin, K. Romanenko, M. Zuev, O. Lapina, Solid state NMR characterization of individual compounds and solid solutions formed in $\text{Sc}_2\text{O}_3\text{-V}_2\text{O}_5\text{-Nb}_2\text{O}_5\text{-Ta}_2\text{O}_5$ system, *Magn. Reson. Chem.* 45 (11) (2007) 962–970.
- [63] A. Flambard, L. Montagne, L. Delevoye, S. Steuernagel, ^{93}Nb and ^{17}O NMR chemical shifts of niobiophosphate compounds, *Solid State Nucl. Magn. Reson.* 32 (2) (2007) 34–43.
- [64] J. Hendrickson, P. Bray, Nuclear magnetic resonance studies of ^7Li ionic motion in alkali silicate and borate glasses, *J. Chem. Phys.* 61 (7) (1974) 2754–2764.
- [65] D. Holland, Y. Iqbal, P. James, B. Lee, Early stages of crystallisation of lithium disilicate glasses containing P_2O_5 – An NMR study, *J. Non Cryst. Solids* 232 (234) (1998) 140–146.
- [66] X. Lu, O. Lafon, J. Trébosc, J.-P. Amoureux, Detailed analysis of the S-RESPDOR solid-state NMR method for inter-nuclear distance measurement between spin-1/2 and quadrupolar nuclei, *J. Magn. Reson.* 215 (2012) 34–49.
- [67] N.T. Duong, F. Rossi, M. Makrinič, A. Goldbourt, M.R. Chierotti, R. Gobetto, Y. Nishiyama, Accurate ^1H - ^{14}N distance measurements by phase-modulated RESPDOR at ultra-fast MAS, *J. Magn. Reson.* 308 (2019), 106559.
- [68] R.W. Dorn, A.L. Paterson, I. Hung, P.L. Gor'kov, A.J. Thompson, A.D. Sadow, Z. Gan, A.J. Rossini, Dipolar heteronuclear correlation solid-state NMR experiments between half-integer quadrupolar nuclei: the case of ^{11}B - ^{17}O , *J. Phys. Chem. C* 126 (28) (2022) 11652–11666.
- [69] Z. Gan, Measuring multiple carbon–nitrogen distances in natural abundant solids using R-RESPDOR NMR, *Chem. Commun.* 45 (2006) 4712–4714.
- [70] L. Chen, X. Lu, Q. Wang, O. Lafon, J. Trébosc, F. Deng, J.-P. Amoureux, Distance measurement between a spin-1/2 and a half-integer quadrupolar nuclei by solid-state NMR using exact analytical expressions, *J. Magn. Reson.* 206 (2) (2010) 269–273.
- [71] F.A. Perras, Z. Wang, T. Kobayashi, A. Baiker, J. Huang, M. Pruski, Shedding light on the atomic-scale structure of amorphous silica–alumina and its Brønsted acid sites, *Phys. Chem. Chem. Phys.* 21 (35) (2019) 19529–19537.
- [72] A. Pedone, G. Malavasi, M.C. Menziani, A.N. Cormack, U. Segre, A new self-consistent empirical interatomic potential model for oxides, silicates, and silica-based glasses, *J. Phys. Chem. B* 110 (24) (2006) 11780–11795.
- [73] T. Otsuka, M.R. Cicconi, D. Dobesh, B. Schroeder, T. Hayakawa, ^{93}Nb NMR study of (K, Na)NbO₃-Doped SiO₂-Na₂O-Al₂O₃ glasses, *Phys. Status Solidi B* (2022), 2200016.